



HAL
open science

Colorimetric assay for the detection of dopamine using bismuth ferrite oxide (Bi₂Fe₄O₉) nanoparticles as an efficient peroxidase-mimic nanozyme

Mehri Razavi, Alexandre Barras, Madjid Ifires, Abir Swaidan, Maryam Khoshkam, Sabine Szunerits, Mohsen Kompany-Zareh, Rabah Boukherroub

► To cite this version:

Mehri Razavi, Alexandre Barras, Madjid Ifires, Abir Swaidan, Maryam Khoshkam, et al.. Colorimetric assay for the detection of dopamine using bismuth ferrite oxide (Bi₂Fe₄O₉) nanoparticles as an efficient peroxidase-mimic nanozyme. *Journal of Colloid and Interface Science*, 2022, 613, pp.384-395. 10.1016/j.jcis.2022.01.041 . hal-03561673

HAL Id: hal-03561673

<https://hal.science/hal-03561673>

Submitted on 22 Jul 2024

HAL is a multi-disciplinary open access archive for the deposit and dissemination of scientific research documents, whether they are published or not. The documents may come from teaching and research institutions in France or abroad, or from public or private research centers.

L'archive ouverte pluridisciplinaire **HAL**, est destinée au dépôt et à la diffusion de documents scientifiques de niveau recherche, publiés ou non, émanant des établissements d'enseignement et de recherche français ou étrangers, des laboratoires publics ou privés.



Distributed under a Creative Commons Attribution - NonCommercial 4.0 International License

1 **Colorimetric assay for the detection of dopamine using**
2 **bismuth ferrite oxide (Bi₂Fe₄O₉) nanoparticles as an**
3 **efficient peroxidase-mimic nanozyme**

4
5 Mehri Razavi^{a,b}, Alexandre Barras^b, Majdid Ifires^{b,c}, Abir Swaidan^b, Maryam Khoshkam^d,
6 Sabine Szunerits^b, Mohsen Kompany-Zareh^{a,e}, Rabah Boukherroub^{b*}

7
8
9
10 *^aDepartment of Chemistry, Institute for Advanced Studies in Basic Sciences, 45137-66731,*
11 *Zanjan, Iran*

12 *^bUniv. Lille, CNRS, Centrale Lille, Univ. Polytechnique Hauts-de-France, UMR 8520 -*
13 *IEMN, F-59000 Lille, France*

14 *^cResearch Center of Semi-conductor Technology for Energy, CRTSE - 02, Bd. Dr. Frantz*
15 *FANON, B.P. 140 Algiers-7, Merveilles 16038, Algeria*

16 *^dDepartment of Chemistry, Faculty of Science, Mohaghegh Ardabili University, 56199-*
17 *11367, Ardabil, Iran*

18 *^eDepartment of Chemistry, Dalhousie University, 6274 Coburg Road, P.O. Box 15000,*
19 *Halifax NS B3H 4R2, Canada*

20
21
22 *Corresponding author: Rabah Boukherroub

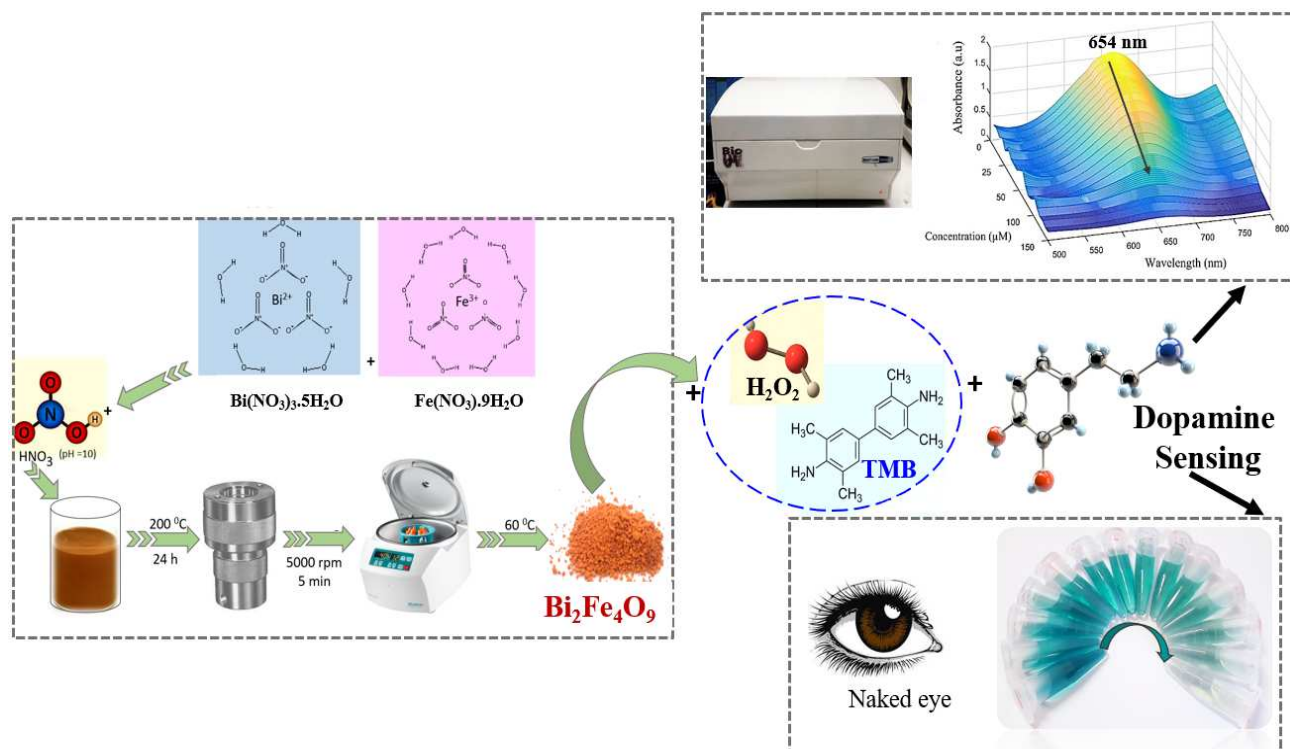
23 Univ. Lille, CNRS, Centrale Lille, Univ. Polytechnique Hauts-de-France, UMR 8520 -
24 IEMN, F-59000 Lille, France

25 Tel: +33362531724; Fax: +33362531701

26 E-mail: rabah.boukherroub@univ-lille.fr

27

Graphical Abstract



29

30

31

32

33

34

35

36

37 Highlights

- 38 ➤ $\text{Bi}_2\text{Fe}_4\text{O}_9$ nanozyme as a simple and low-cost colorimetric sensor was developed for easy
- 39 dopamine detection
- 40 ➤ The sensor achieved good performance with a linear range from 0.15 to $50\text{ }\mu\text{M}$ and a
- 41 detection limit of 51 nM
- 42 ➤ The nanozyme was reused up to 4 cycles without a significant decrease in its performance

43

44 **Abstract**

45 This work describes the preparation of ternary bismuth ferrite oxide nanoparticles ($\text{Bi}_2\text{Fe}_4\text{O}_9$
46 NPs) with an enzyme mimetic activity for dopamine (DA) qualitative and quantitative
47 detection. $\text{Bi}_2\text{Fe}_4\text{O}_9$ NPs were prepared using a facile, low cost, and one-pot hydrothermal
48 treatment. The chemical composition, morphology, and optical properties of $\text{Bi}_2\text{Fe}_4\text{O}_9$
49 nanozyme were characterized using different techniques such as Fourier-transform infrared
50 spectra (FTIR), X-ray diffraction pattern (XRD), X-ray photoelectron spectroscopy (XPS),
51 thermo-gravimetric analysis (TGA), dynamic light scattering (DLS), field-emission scanning
52 electron microscopy (FESEM) imaging, FESEM-energy dispersive X-ray spectroscopy
53 (EDS), UV-vis absorption, and fluorescence emission spectroscopy. $\text{Bi}_2\text{Fe}_4\text{O}_9$ NPs were
54 utilized to catalyze the oxidation of a typical chromogenic peroxidase substrate, 3,3',5,5'-
55 tetramethylbenzidine (TMB), to form the blue-colored oxidized product (oxTMB), in the
56 presence of hydrogen peroxide (H_2O_2). All reactions occurred in acetate buffer solution (pH
57 3.5) to generate hydroxyl radicals ($\cdot\text{OH}$) and the kinetics were followed by UV-vis
58 absorbance at 654 nm. The steady-state kinetic parameters were obtained from the Michaelis-
59 Menten equation and exhibited a good catalytic efficiency of $\text{Bi}_2\text{Fe}_4\text{O}_9$ NPs as enzyme
60 mimetics. Michaelis–Menten constant (K_m) values were estimated as 0.07 and 0.73 mM for
61 TMB and H_2O_2 , respectively. The presented method is efficient, rapid, cost-effective, and
62 sensitive for the colorimetric detection of dopamine with a linear range (LR) from 0.15 to 50
63 μM and a detection limit (LOD) of 51 nM. The proposed colorimetric sensor was
64 successfully applied for the detection of different concentrations of dopamine in spiked fetal
65 bovine serum (FBS) and horse serum (HS) samples. It is anticipated that $\text{Bi}_2\text{Fe}_4\text{O}_9$ nanozyme
66 holds great potential in biomedical analysis and diagnostic applications of dopamine-related
67 diseases.

68

69

70

71

72

73 **Keywords:** $\text{Bi}_2\text{Fe}_4\text{O}_9$ nanozyme, 3,3',5,5'-tetramethylbenzidine (TMB), Peroxidase-like
74 activity, Dopamine, Colorimetric assay.

75

76

77

78 **1. Introduction**

79 Dopamine (DA), 4-(2-aminoethyl) benzene-1,2-diol), is a biogenic monoamine and one of
80 the quite important catecholamine neurotransmitters (NT), which plays significant key roles
81 in the mammalian central nervous such as memory, learning, cognition, emotions, renal,
82 hormonal, and cardiovascular systems [1-3]. The abnormal level of dopamine concentration
83 in the human body can lead to serious neurological syndromes and various diseases like
84 Alzheimer, Parkinson, Huntington, senile dementia, and Schizophrenia [4-7].

85 Therefore, the measurement of the dopamine level in biological fluids with high accuracy
86 and sensitivity is an extremely important factor for early diagnosis of diseases and
87 development of therapeutic approaches [3, 8]. Various analytical strategies have been
88 developed to detect the DA level, including high-performance liquid chromatography
89 (HPLC) [9], capillary electrophoresis (CE) [10, 11], field-effect transistor (FET)-based
90 biosensor [12], fluorometry [13, 14], random lasers (RL) with incoherent feedback [15],
91 electrochemiluminescence (ECL) [16], and electrochemical methods [17, 18]. However, all
92 these methods have several constraints; they often require complex and advanced pre-
93 treatment processes, long analysis times, high-costs, sophisticated instruments, and trained
94 personnel [4, 8]. In this regard, many studies have been focused on elucidating the
95 colorimetric assays for dopamine identification, because of their intrinsic advantages of
96 simple assay design, time-saving, high efficiency, and most importantly, easy visual detection
97 [3, 4, 7].

98 Traditionally, natural enzymes as biological catalysts have been applied in colorimetric
99 analysis systems. A common example is the horseradish peroxidase enzyme (HRP). To keep
100 up with the more efficient performance of natural enzymes, they must be applied under
101 relatively mild conditions. Natural enzymes feature high substrate-specificity and efficiency.
102 However, they are limited by some inherent drawbacks such as the high-cost of preparation
103 and purification, easy denaturation, the extreme sensitivity of catalytic activity towards
104 environmental changes such as pH or temperature, difficulties in recovery, limited storage,
105 and availability [19, 20]. As a potential alternative, an emerging group of nanomaterials has
106 recently been considered. The choice of enzyme-mimics based on nanomaterials rather than
107 natural enzymes has well-confirmed the rational decision to detect dopamine and conquer
108 these limitations. The significant properties of nanozymes include a high surface-to-volume
109 ratio, low-cost, simple preparation, tunable activity, high stability, long-term storage, and

110 easy preparation. As evidenced by the mentioned advantages, nanozymes have been
111 exploited to further evaluate their analytical performance in bio-nanotechnology [21-23].

112 Yan and colleagues were the first to point out Fe_3O_4 NPs as an enzyme-mimic for TMB
113 substrate [24]. In recent years, ferrite-based enzyme-like nanomaterials have generated
114 tremendous attention [25-27], because of their potential for various applications such as gas
115 sensors [28], catalyst for ammonia oxidation [29], photocatalysts for hydrophobic and
116 organic pollutants degradation [26, 30], removal of heavy metal ions [31], memory devices
117 [32], data storage [33], and spintronic devices [34]. Lu and colleagues successfully
118 synthesized and applied $\text{CuFe}_2\text{O}_4/\text{Cu}_9\text{S}_8/\text{polypyrrole}$ (PPy) ternary nanotubes as a suitable
119 colorimetric platform for easy detection of dopamine and H_2O_2 molecules [35]. Chen et al.
120 reported that Fe/NC-800 exhibited an enhanced catalytic activity for dopamine sensing [36].
121 Liu and co-workers reported that $\text{ZnO}/\text{ZnFe}_2\text{O}_4/\text{graphene foam}$ (ZZFO/GF) is an excellent
122 colorimetric-catalyst to distinguish hydroquinone (HQ) molecules with the assistance of H_2O_2
123 molecule [37]. Su and co-workers demonstrated the use of the spinel ZnFe_2O_4 NP-decorated
124 ZnO nanofiber as an effective colorimetric platform with a peroxidase-like activity for
125 glucose detection in urine samples [38]. Hou et al. fabricated $\text{Fe}_3\text{O}_4@\text{C}@\text{MnO}_2$ composite as
126 a triple-enzyme mimetic activity to catalyze TMB oxidation reaction and was successfully
127 applied for dopamine detection [39].

128 In this investigation, we report, for the first time, the application of irregular sheet-like
129 $\text{Bi}_2\text{Fe}_4\text{O}_9$ nanoparticles as one of the Fe-based nanozymes for the colorimetric detection of
130 nanomolar concentration of dopamine in aqueous media. Fe active sites ($\text{Fe}^{2+}/\text{Fe}^{3+}$) and the d-
131 orbitals of Fe^{3+} in $\text{Bi}_2\text{Fe}_4\text{O}_9$ NPs operate in a Fenton-like reaction to improve the catalytic
132 oxidization of 3,3',5,5'-tetramethylbenzidine (TMB), a chromogenic substrate, in presence of
133 H_2O_2 in acetic acid medium (pH=3.5) to yield a deep-blue product (oxTMB). The
134 simultaneous existence of large irregular-sheets and Fe, as a transition-metal ion, located at
135 FeO_6 (octahedral) and FeO_4 (tetrahedral) in the unit cell of $\text{Bi}_2\text{Fe}_4\text{O}_9$ nanozyme, were useful
136 factors to reduce H_2O_2 to $\cdot\text{OH}$ radical and increase the oxidation of TMB molecules. In
137 presence of dopamine (DA), as efficient $\cdot\text{OH}$ radical scavenger, the colorimetric signal of the
138 $\text{Bi}_2\text{Fe}_4\text{O}_9/\text{H}_2\text{O}_2/\text{TMB}/\text{DA}$ was significantly lower than that of $\text{Bi}_2\text{Fe}_4\text{O}_9/\text{H}_2\text{O}_2/\text{TMB}$ system,
139 and the deep-blue color of the ox-TMB was changed to fade-blue color. On the basis of this
140 quenching behavior, the catalytic activity of $\text{Bi}_2\text{Fe}_4\text{O}_9$ nanozyme was exploited to design a
141 selective and sensitive colorimetric sensor for dopamine concentration determination in fetal
142 bovine serum (FBS) and horse serum (HS) samples. The results of the study showed that

143 Bi₂Fe₄O₉ NPs could be developed as a promising group of nanozyme materials for dopamine
144 diagnostic purposes and biomedical applications.

145 **2. Experimental**

146 *2.1. Synthesis of Bi₂Fe₄O₉ nanoparticles*

147 As shown in **Scheme S1**, Bi₂Fe₄O₉ NPs were prepared using the hydrothermal method,
148 according to a previous procedure with a slight modification [27]. First, Bi(NO₃)₃·5H₂O (4.85
149 g) and Fe(NO₃)₃·9H₂O (4.04 g) powders were dissolved in 13 mL of deionized water (DIW)
150 and 2 mL of nitric acid (HNO₃ 65%) at room temperature (RT) to form solution A.
151 Throughout the process, the above solution was kept under vigorous magnetic stirring for 30
152 min. Then, 75 mL of potassium hydroxide (KOH, 8 M) as a mineralizer was slowly dropped
153 into solution A to adjust the pH to 8-9 with rapid stirring. It is worth noticing that a red-
154 brown suspension of a bismuth-ferrite was formed at room temperature. In hydrothermal
155 processing, the uniform suspension was transferred into a Teflon-lined autoclave and heated
156 at 200 °C for 24 h. Then, the autoclave was cooled to room temperature and the formed
157 precipitate was collected by centrifugation at 5,000 rpm for 5 min and washed at least three
158 times with deionized water and ethanol (95%) to remove residual ions. Furthermore, the
159 produced Bi₂Fe₄O₉ powder was dried in an oven at 60 °C overnight for later use. Ultimately,
160 the produced Bi₂Fe₄O₉ NPs were yellow-orange color at room temperature.

161

162 *2.2. Peroxidase-like activity of Bi₂Fe₄O₉ nanoparticles*

163 In a typical assay, different concentrations of Bi₂Fe₄O₉ (0-30 µg/mL) were added to 225
164 µL of TMB (0.3 mM dissolved in ethanol), 225 µL of H₂O₂ (5 mM) in acetate buffer (pH 3.5,
165 0.1 M) and the final volume of solution was adjusted to 1.5 mL. The mixture was incubated
166 for 25 min at 45 °C. All chemical reagents were exactly prepared before every experiment.
167 UV-vis spectrometry (500 to 800 nm) was used to investigate the absorbance variation at 654
168 nm due to oxidation of TMB substrate.

169

170 *2.3. Steady-state kinetics for the determination K_m and V_{max}*

171 The catalytic efficiency and the rate of enzyme reactions of Bi₂Fe₄O₉ NPs can be
172 determined by the Michaelis–Menten equation. To assess the kinetics parameters, the
173 utilization of different substrate concentrations (TMB or H₂O₂) is an essential factor. Under
174 the optimized conditions, kinetic experiments were determined by adding various
175 concentrations of TMB chromogenic substrate (0.01-0.30 mM) at a fixed concentration of

176 H₂O₂ (5 mM) in the first set of experiments. For the second set of kinetic experiments, the
177 H₂O₂ concentration was varied from 0.1 to 5.0 mM while the concentration of TMB substrate
178 was kept constant (0.3 mM). All experiments were carried out in the acetic acidic buffer (pH
179 3.5, 0.1 M) and the total volume of the mixture solutions was equal to 1.5 mL. UV-vis
180 absorbance was recorded within the 500-800 nm range and the obtained V_{max}, and K_m values
181 were compared with the kinetic parameters of other nanozymes.

182

183 *2.4. Colorimetric assay for the detection of dopamine*

184 To accurately investigate the efficacy of Bi₂Fe₄O₉ NPs (120 μL, 8 μg/mL) to detect
185 dopamine, first, a solution of a fixed concentration of TMB (225 μL, 0.3 mM) and H₂O₂ (525
186 μL, 5 mM) in acetate buffer solution (pH=3.5, 0.1 M) was prepared. Afterward, various
187 dopamine concentrations (0-150 μM) were added to the above solution; the total volume was
188 1.5 mL. The entire reaction mixture was quickly shaken then incubated at 45 °C for 25 min.
189 The course of the reaction was monitored using UV-vis spectrometer (500-800 nm). At the
190 end of incubation, UV-vis absorbance values were recorded at 654 nm and the obtained
191 maximum absorbance was used to generate the calibration curve and also to determine the
192 limit of detection of dopamine.

193

194 *2.5. Selectivity and reproducibility of Bi₂Fe₄O₉ nanoparticles*

195 To evaluate the selectivity of the designed colorimetric assay, various amino acids and
196 small molecules such as alanine (Ala), cysteine (Cys), arginine (Arg), lysine (Lys),
197 glutathione (GSH), uric acid (UA), ascorbic acid (AA), lactose (Lac), glucose (Glu), fructose
198 (Fru), and different ions (K⁺, Na⁺, Mg²⁺, and Ca²⁺) were separately added to the mixture
199 solution of TMB (0.3 mM), H₂O₂ (5 mM), and Bi₂Fe₄O₉ NPs (8 μg/mL) in acetate buffer (pH
200 3.5, 0.1 M). The concentration of applied interfering components was two times the
201 concentration of dopamine (100 μM). All the above solutions were incubated for 25 min at
202 45 °C, and their UV-vis spectra were measured in the 500-800 nm range. The characteristic
203 reproducibility of the synthesized Bi₂Fe₄O₉ nanozyme was examined for four catalytic cycles
204 of TMB oxidation under the optimized experimental conditions (Bi₂Fe₄O₉ (8 μg/mL), TMB
205 (0.3 mM), H₂O₂ (5 mM), acetate buffer (pH 3.5, 0.1 M), T=45 °C, and incubation time=25
206 min).

207

208 *2.6. Procedure for dopamine detection in real samples*

209 For dopamine analysis in real samples, 1 μ L of pure fetal bovine serum (FBS) and horse
210 serum (HS) samples were diluted in phosphate buffer saline (PBS pH 7.4) and then $\text{Bi}_2\text{Fe}_4\text{O}_9$
211 nanozyme (8 $\mu\text{g}/\text{mL}$), H_2O_2 (5 mM), and TMB (0.3 mM) were added. The total volume of
212 the solution was maintained at 1.5 mL using acetate buffer (pH 3.5, 0.1 M). Afterward,
213 different concentrations of dopamine (1, 5, and 10 μM) were introduced into the above
214 mixture solution and incubated for 25 min at 45 $^\circ\text{C}$. To detect the presence of dopamine in the
215 FBS 1 (Sigma-Aldrich), FBS (Fisher Scientific), and HS (Fisher Scientific) samples, the
216 corresponding changes in the absorbance spectra were monitored by UV-vis spectroscopy
217 (500-800 nm). All experiments were performed in triplicates.

218

219 *2.7. Detection of hydroxyl radicals ($\cdot\text{OH}$) generation in the presence of $\text{Bi}_2\text{Fe}_4\text{O}_9$*

220 In a typical assay, 0.2 mM of terephthalic acid (TA) was dissolved in ethanol. Eight
221 mixtures were prepared as following: (a) H_2O_2 (5 mM) + $\text{Bi}_2\text{Fe}_4\text{O}_9$ NPs (8 $\mu\text{g}/\text{mL}$), (b) H_2O_2
222 (5 mM) + $\text{Bi}_2\text{Fe}_4\text{O}_9$ NPs (8 $\mu\text{g}/\text{mL}$) + dopamine (50 μM), (c) $\text{Bi}_2\text{Fe}_4\text{O}_9$ NPs (8 $\mu\text{g}/\text{mL}$), (d)
223 $\text{Bi}_2\text{Fe}_4\text{O}_9$ NPs (8 $\mu\text{g}/\text{mL}$) + dopamine (50 μM), (e) H_2O_2 (5 mM), (f) H_2O_2 (5 mM) +
224 dopamine (50 μM), (g) only TA (15 μl), and (h) TA (15 μl) + dopamine (50 μM) in acetate
225 buffer (pH 3.5), and all solutions were incubated for 25 min at 45 $^\circ\text{C}$. The total volume of
226 eight tubes was filled to 1.5 mL. The change of fluorescence emission spectra ($\lambda_{\text{ex}}=315$ nm)
227 was recorded in the 400–550 nm range by utilizing a Safas Xenius XC fluorescence
228 spectrophotometer.

229 Moreover, to examine the presence of $\cdot\text{OH}$ radicals as one of the members of reactive
230 oxygen species (ROS), *tert*-butyl alcohol (TBA) was used as a quencher. $\text{Bi}_2\text{Fe}_4\text{O}_9$ NPs (8
231 $\mu\text{g}/\text{mL}$), TMB (0.3 mM), H_2O_2 (5 mM), acetate buffer (pH 3.5, 0.1 M), TBA (0.5 mM) were
232 incubated at 45 $^\circ\text{C}$ for 25 min (total volume of the solution was 1.5 mL). All absorption
233 spectra of the solutions with or without TBA molecules were recorded at 564 nm.

234

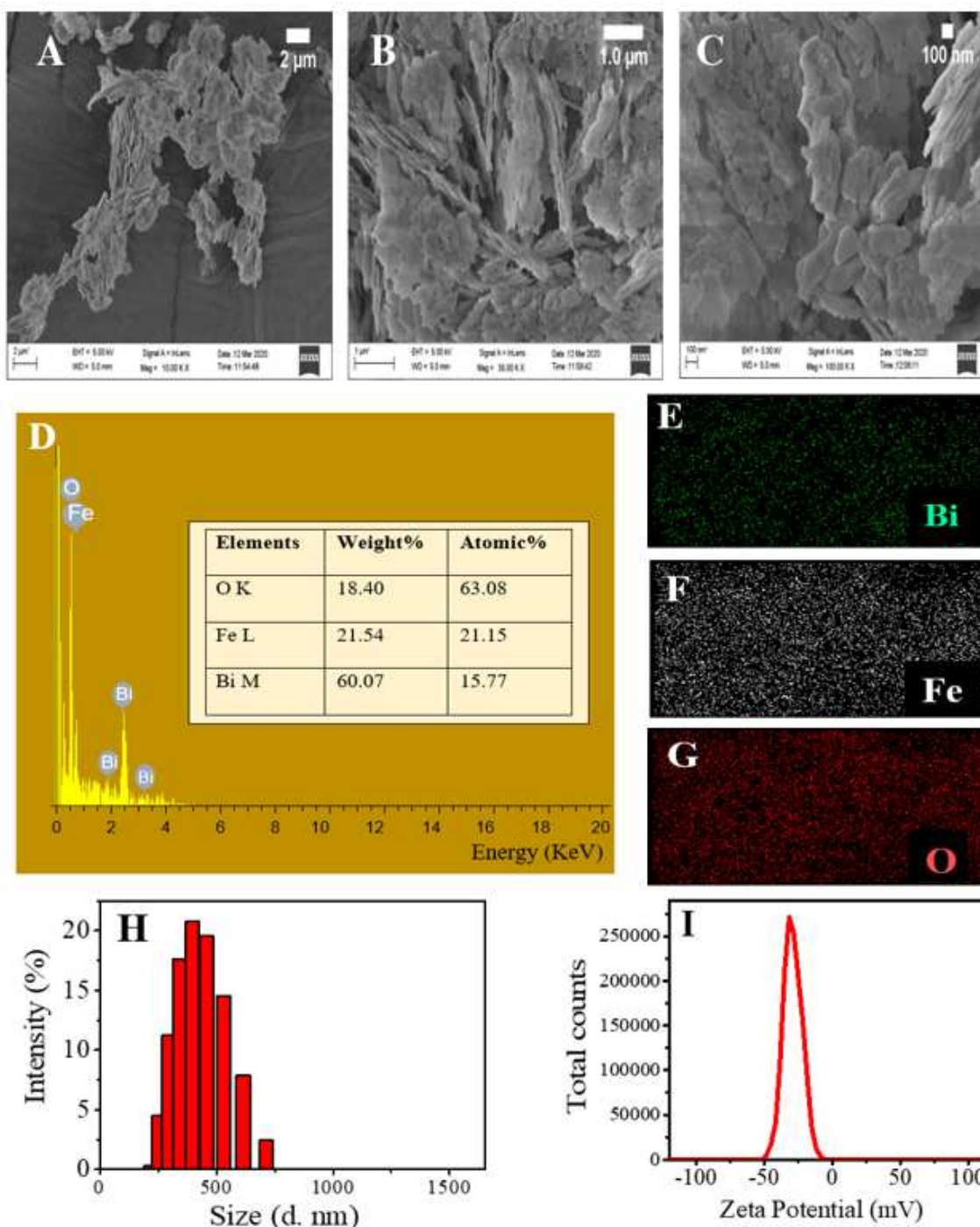
235 **3. Results and discussion**

236 *3.1. Characterization of $\text{Bi}_2\text{Fe}_4\text{O}_9$ nanoparticles*

237 As observed in **Fig. 1**, the morphological and chemical composition of the as-prepared
238 $\text{Bi}_2\text{Fe}_4\text{O}_9$ nanozyme were characterized by field emission scanning electron microscopy
239 (FESEM) imaging and energy-dispersive X-ray (EDX) spectroscopy. The low and high
240 magnification FESEM micrographs showed that $\text{Bi}_2\text{Fe}_4\text{O}_9$ consist of an irregularly sheet-like
241 morphology (**Fig. 1A-C**).

242 The accumulation of initial bismuth and ferrite salts causes the random collision of Bi-Fe-
243 O elements, which leads to an increase of the irregular sheet growth. The irregular particle
244 shapes of $\text{Bi}_2\text{Fe}_4\text{O}_9$ were formed by considering the different growth rates in various
245 directions. Taken together, the results of elemental distribution mapping and EDX analysis
246 (**Fig. 1D**) clearly illustrate the presence of Bi, Fe, and O elements, which is in full agreement
247 with the chemical composition of $\text{Bi}_2\text{Fe}_4\text{O}_9$ NPs. The atomic percentages of Bi, Fe, and O
248 elements in the $\text{Bi}_2\text{Fe}_4\text{O}_9$ sample were equal to 15.77%, 21.15%, and 63.08%, respectively. It
249 can be noticed that there is a deviation from the stoichiometric composition due to iron
250 deficiency. As revealed in **Fig. 1E-G**, the elemental mapping of Bi (green), Fe (white), and O
251 (red) has intelligibly confirmed the uniform distribution of mentioned elements on the surface
252 of $\text{Bi}_2\text{Fe}_4\text{O}_9$ enzyme-mimicking nanomaterial [27, 31].

253 The hydrodynamic radius and particle size distributions of the synthesized $\text{Bi}_2\text{Fe}_4\text{O}_9$ NPs
254 were measured by utilizing the dynamic light scattering (DLS) and zeta potential techniques,
255 respectively (**Fig. 1H and I**). The average hydrodynamic diameter (d_{hydr}) of $\text{Bi}_2\text{Fe}_4\text{O}_9$ NPs
256 was ~ 396 nm (3 measurements). In addition, the surface charge of $\text{Bi}_2\text{Fe}_4\text{O}_9$ was found to be
257 -31.62 mV. Based on these results, $\text{Bi}_2\text{Fe}_4\text{O}_9$ NPs with a negative surface charge are expected
258 to interact electrostatically with the positively charged chromogenic substrate (TMB) and
259 efficiently catalyze the oxidation of TMB. The positive surface charge of TMB was brought
260 by the presence of two amine groups [40-42].



261
 262 **Fig. 1.** FESEM images at low and high magnifications (A-C), EDX spectrum (D), elemental
 263 mappings for Bi (E), Fe (F), and O (G), DLS size distribution (H), and zeta potential (I) of
 264 the as-prepared Bi₂Fe₄O₉ NPs.

265
 266 **Fig. S1** depicts the FTIR spectrum of the Bi₂Fe₄O₉ NPs (700-4000 cm⁻¹), which indicates
 267 the presence of diverse functional groups on the surface of the NPs. The spectrum comprises
 268 broad and weak absorption bands at 3441 and 1636 cm⁻¹ related to hydroxyl groups
 269 stretching and bending vibrations from water molecules or intermolecular hydrogen bonds,

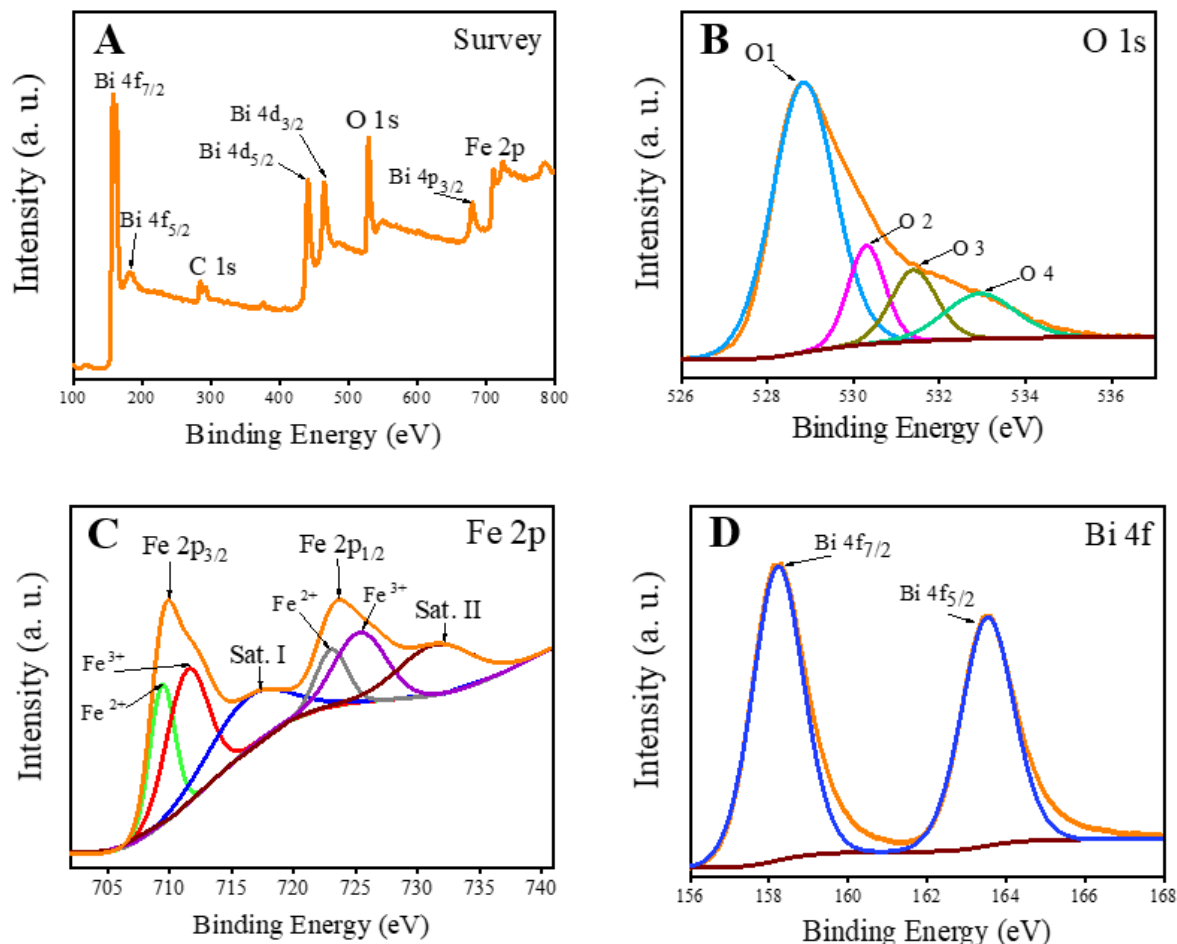
270 respectively. The strong absorption peak at 1384 cm^{-1} belongs to the residual NO_3^- group
271 incorporated during the preparation of $\text{Bi}_2\text{Fe}_4\text{O}_9$ sample. Besides, bismuth ferrite is an
272 isostructural compound and contains tetrahedral FeO_4 , octahedral FeO_6 , and octahedral BiO_6
273 units. The vibration band at 808 cm^{-1} is assigned to Fe-O stretching vibrations of FeO_4 and
274 FeO_6 , and also Bi-O in the BiO_6 octahedral pairs [31, 43, 44].

275 The results of the thermogravimetric analysis (TGA) and derivative thermogravimetric
276 (DTG) of $\text{Bi}_2\text{Fe}_4\text{O}_9$ NPs in the 30–980 °C temperature range are shown in **Fig. S2**. TGA
277 analysis of $\text{Bi}_2\text{Fe}_4\text{O}_9$ NPs demonstrates four clear steps of weight loss: (I) 50 °C, (II) 150 °C,
278 (III) 220 °C, (IV) 657 °C corresponding to the mass reduction of 0.79%, 0.79%, 0.47% and
279 5.49%, respectively. The first step belongs to water and residual organic solvent evaporation,
280 and the second step of the significant mass loss was probably due to the decomposition of the
281 ternary metal oxide structure of BFO [45]. By increasing the temperature (978.5 °C), the
282 TGA curve of $\text{Bi}_2\text{Fe}_4\text{O}_9$ features an approximate loss of 8.21% of its total mass and 91.79%
283 of the residual mass was left at the end of heating.

284 X-ray photoelectron spectrometry (XPS) was utilized to examine the elemental
285 composition and the oxidation states of the as-prepared $\text{Bi}_2\text{Fe}_4\text{O}_9$ NPs (**Fig. 2A-D**). The XPS
286 survey spectrum of $\text{Bi}_2\text{Fe}_4\text{O}_9$ NPs revealed the presence of Bi 4f, Bi 4d, Bi 4p, C 1s, Fe 2p,
287 and O 1s peaks (**Fig. 2A**). In the survey spectrum of $\text{Bi}_2\text{Fe}_4\text{O}_9$ NPs (**Fig. 2A**), the narrow peak
288 of C 1s observed at 285 eV is most likely due to surface contamination. On the basis of the
289 XPS results, the atomic percentages of Bi, Fe, and O elements in $\text{Bi}_2\text{Fe}_4\text{O}_9$ NPs were 13.72,
290 17.62, and 68.66 at.%, respectively. The results reflect Fe deficiency, in accordance with
291 EDX analysis, even though there was no evidence for the existence of another crystalline
292 phase (see XRD analysis below).

293 The O 1s wide scan spectrum (**Fig. 2B**) can be fitted with four Gaussian curves at around
294 528.8 eV (O1), 530.3 eV (O2), 531.4 eV (O3), and 532.9 eV (O4), which are respectively
295 ascribed to lattice M–O–M bonds, surface lattice oxygen, the presence of oxygen vacancies,
296 and absorbed H_2O or surface carbonate [27, 46, 47]. As shown in **Fig. 2C**, the wide scan of
297 Fe 2p XPS profile can be fitted with two components at binding energies of 710.1 and 723.6
298 eV, that are respectively assigned to Fe $2p_{3/2}$ and Fe $2p_{1/2}$. These binding energies data
299 confirmed the occurrence of two oxidation states (+2 and +3) in the BFO oxide. The high-
300 resolution spectrum of Fe $2p_{3/2}$ can be deconvoluted into two Gaussian peaks at 711.4 and
301 725.4 eV which belong to the Fe^{3+} valence state in the $\text{Bi}_2\text{Fe}_4\text{O}_9$. The two peaks at 709.4 and
302 723.1 eV can be attributed to Fe $2p_{1/2}$ that correlate with the existence of Fe^{2+} ions in Fe-O
303 bands. Furthermore, the two satellite peaks located at 717.9 eV (Sat. I) and 732.2 eV (Sat. II)

304 both belong to Fe^{3+} species in the $\text{Bi}_2\text{Fe}_4\text{O}_9$ NPs [27, 47-49]. The Bi 4f XPS plot (**Fig. 2D**)
 305 can be deconvoluted into two distinct peaks ascribed to Bi 4f_{7/2} peak at 158.2 eV and Bi 4f_{5/2}
 306 peak at 164.1 eV. The spin-orbit splitting of Bi 4f (5.90 eV) corresponds to bismuth ion in the
 307 +3-valence state in the synthesized $\text{Bi}_2\text{Fe}_4\text{O}_9$ NPs [26, 27, 50].



308
 309 **Fig. 2.** (A) XPS survey spectrum, and high-resolution XPS spectra of (B) O 1s, (C) Fe 2p,
 310 and (D) Bi 4f regions of $\text{Bi}_2\text{Fe}_4\text{O}_9$ NPs.

311 The phase purity and crystallinity of the as-prepared $\text{Bi}_2\text{Fe}_4\text{O}_9$ NPs were analyzed by X-
 312 ray diffraction (XRD) patterns (**Fig. S3**). The characteristic diffraction peaks located at 2θ
 313 angles of 14.78° , 20.88° , 22.40° , 23.88° , 24.90° , 25.72° , 26.88° , 28.06° , 28.94° , 29.72° ,
 314 30.80° , 33.58° , 35.52° , 36.62° , 37.54° , 39.20° , 44.18° , 45.40° , 46.82° , 48.82° , 49.50° , 50.68° ,
 315 52.04° , 54.36° , 55.30° , 56.54° , 58.8° , 61.56° , 64.68° , and 67.22° can be perfectly indexed to
 316 the orthorhombic $\text{Bi}_2\text{Fe}_4\text{O}_9$ structure with (001), (020), (200), (120), (210), (021), (201),
 317 (121), (211), (002), (220), (130), (310), (022), (202), (212), (140), (132), (141), (240), (411),
 318 (420), (123), (142), (402), (332), (431), (004), (342), and (530), respectively ((JCPDS File
 319 No. 00-025-0090). The crystalline planes with d-spacing values related to the above crystal

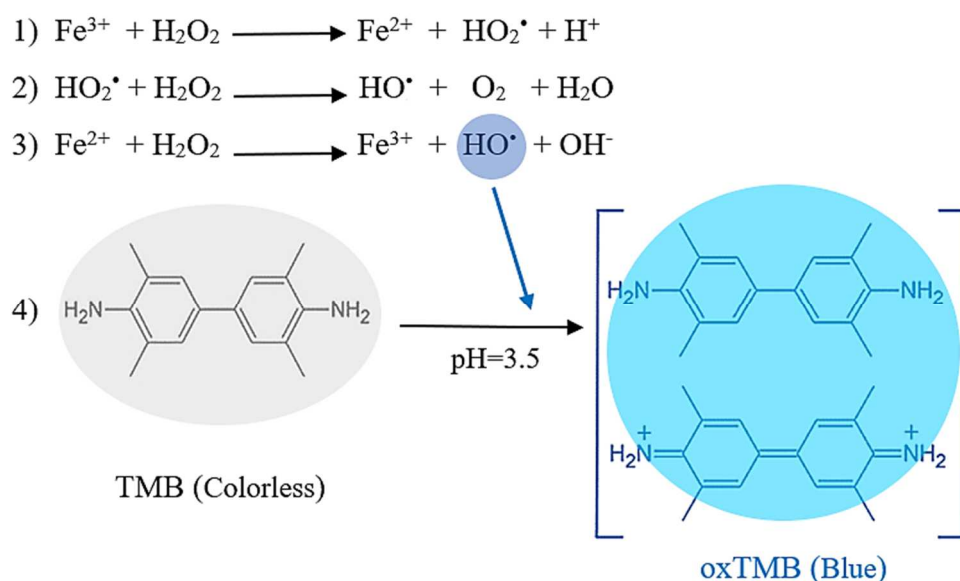
320 planes of $\text{Bi}_2\text{Fe}_4\text{O}_9$ sample were determined to be 5.99, 4.25, 3.97, 3.72, 3.57, 3.46, 3.32,
321 3.18, 3.09, 3.00, 2.90, 2.67, 2.52, 2.45, 2.39, 2.30, 2.05, 2.00, 1.93, 1.86, 1.83, 1.80, 1.75,
322 1.68, 1.65, 1.63, 1.57, 1.51, 1.44, and 1.39 Å, respectively. The sharp diffraction peaks in the
323 XRD pattern obviously indicate that $\text{Bi}_2\text{Fe}_4\text{O}_9$ has a well-crystallized structure without the
324 existence of other impurities [44, 51-53]

325

326 *3.2. Peroxidase-like activity of $\text{Bi}_2\text{Fe}_4\text{O}_9$ nanoparticles*

327 In this catalytic process, the enzyme-mimetic activity of $\text{Bi}_2\text{Fe}_4\text{O}_9$ NPs was examined for
328 the oxidation of TMB, as electron-donor species, to ox-TMB in the presence of H_2O_2 as
329 electron-acceptor species. The decomposition of H_2O_2 molecules was catalyzed by Fe species
330 on the surface of $\text{Bi}_2\text{Fe}_4\text{O}_9$ nanozyme. Ferrite ions in $\text{Bi}_2\text{Fe}_4\text{O}_9$ nanozyme are located at FeO_6
331 octahedral and FeO_4 tetrahedral in the unit cell. Fe is a useful transition metal ion in Fenton
332 reactions to reduce H_2O_2 to $\cdot\text{OH}$ radicals. Different oxidation forms of Fe cations like
333 $\text{Fe}^{3+}/\text{Fe}^{2+}$ and the d-orbitals of Fe^{3+} were consecutively produced and used in the suggested
334 Fenton-reaction cycle. Besides the Fe active-sites, the large irregular sheet area of $\text{Bi}_2\text{Fe}_4\text{O}_9$
335 created more reactive sites and enhanced the peroxidase-like activity of $\text{Bi}_2\text{Fe}_4\text{O}_9$ nanozyme.
336 To mimic the Fenton-like reaction, Fe ions and the produced $\cdot\text{OH}$ radicals played a key role
337 in oxidizing TMB molecules to the blue-coloured form of TMB semiquinone dimer [43, 44,
338 47, 54-58].

339 TMB oxidation in presence of $\text{Bi}_2\text{Fe}_4\text{O}_9$ nanozyme is believed to occur through a Fenton-
340 like reaction, as summarized in **Eq. 1-4 (Scheme 1)**. In a weakly acidic medium, $\text{Bi}_2\text{Fe}_4\text{O}_9$
341 nanozyme successfully decomposes H_2O_2 molecules to hydroxyl radical ($\cdot\text{OH}$), as an
342 effective intermediate molecule (**Eq. 3**) to carry out the oxidation of TMB molecules in
343 $\text{H}_2\text{O}_2/\text{TMB}/\text{Bi}_2\text{Fe}_4\text{O}_9$ system (**Eq. 4**) at room temperature. The oxidized TMB substrate can
344 be visualized by monitoring the maximum absorbance peak at 654 nm.

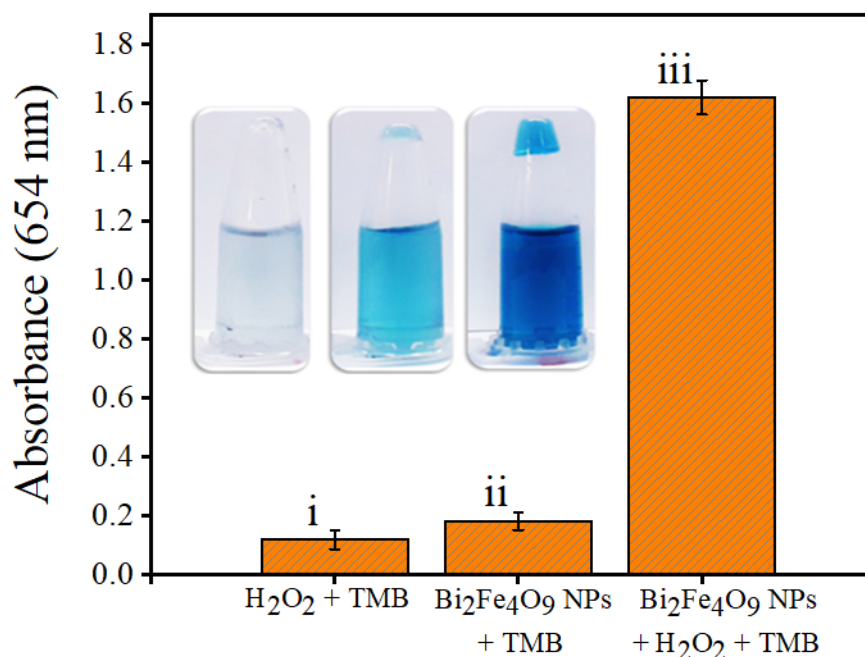


345

346 **Scheme 1.** Schematic illustration of the plausible mechanism of TMB oxidation by H_2O_2 in
 347 the presence of $\text{Bi}_2\text{Fe}_4\text{O}_9$ NPs.

348

349 Under the reaction conditions, the meaningful effect of the absence and presence of
 350 $\text{Bi}_2\text{Fe}_4\text{O}_9$ nanozyme catalyst and H_2O_2 molecule on the catalytic oxidation of TMB substrate
 351 was investigated and the variation of UV-vis spectra are displayed in **Fig. 3(i-iii)**. Insert in
 352 **Fig. 3** indicated the recorded photographs of the oxTMB color-change system. The
 353 experimental systems consisting of only H_2O_2 or $\text{Bi}_2\text{Fe}_4\text{O}_9$ had no obvious effect on the
 354 oxidation reaction of TMB and the absorbance signal of the solutions was close to the
 355 background (**Fig. 3i**). Meanwhile, the addition of $\text{Bi}_2\text{Fe}_4\text{O}_9$ to TMB only slightly increased
 356 the TMB oxidation (**Fig. 3ii**). After the introduction of both $\text{Bi}_2\text{Fe}_4\text{O}_9$ and H_2O_2 solutions into
 357 the fresh TMB reagent, the peroxidase-like activity $\text{Bi}_2\text{Fe}_4\text{O}_9$ improved and considerably
 358 decomposed H_2O_2 molecules to $\bullet\text{OH}$ as active intermediates for oxidation of TMB (**Fig. 3iii**).
 359 In an acidic medium (pH 3.5), the occurrence of the oxidation reaction was confirmed by the
 360 naked eyes through the color change from the colorless mixtures of $\text{H}_2\text{O}_2/\text{TMB}$ and
 361 $\text{Bi}_2\text{Fe}_4\text{O}_9/\text{TMB}$ to the deep-blue color of $\text{H}_2\text{O}_2/\text{TMB}/\text{Bi}_2\text{Fe}_4\text{O}_9$, and also the produced ox-
 362 TMB recorded a remarkable absorbance at around 654 nm (**Fig. 3**). All of the results
 363 demonstrated that the presence of both $\text{Bi}_2\text{Fe}_4\text{O}_9$, as intrinsic peroxidase-like activity catalyst,
 364 and H_2O_2 , as inherent oxidant, was responsible for the remarkable increase of the oxidation
 365 rate of TMB substrate.



366

367 **Fig. 3.** Relative UV–vis absorption spectra changes of different solutions containing acetate
 368 buffer (pH 3.5, 0.1 M) and reaction components recorded after 25 min incubation at T=45 °C.
 369 Typical photographs of the oxidized TMB (oxTMB) [from left to right: (i) H₂O₂+TMB
 370 without Bi₂Fe₄O₉ NPs (colorless), (ii) TMB+Bi₂Fe₄O₉ without H₂O₂ (slightly blue), and (iii)
 371 TMB+ H₂O₂+Bi₂Fe₄O₉ NPs (blue)]. Reaction condition: Bi₂Fe₄O₉ NPs (8 μg/mL), TMB (0.3
 372 mM), H₂O₂ (5 mM), T=45 °C (For each solution, n=3).

373 3.3. Experimental condition optimization

374 In order to have a better insight into the reaction performance, the enzyme-like catalytic
 375 reaction was performed under different experimental conditions by varying TMB, H₂O₂, and
 376 Bi₂Fe₄O₉ concentrations, pH, temperature, and the incubation time of the reaction [24, 59].
 377 The effects of the different concentrations of Bi₂Fe₄O₉ NPs (1-30 μg/mL), TMB (0-0.7 mM),
 378 and H₂O₂ (0-8 mM), pH (pH=1-12), incubation time (5-50 min), and temperature (15-60 °C)
 379 was investigated and clearly depicted in **Fig. S4A-F**. Optimizing the concentrations of
 380 Bi₂Fe₄O₉, TMB, and H₂O₂ molecules were manifested by the maximum value of absorbance
 381 at 654 nm. As depicted in **Fig. S4A-C**, the optimum absorbance was recorded using 8 μg/mL,
 382 0.3 mM, and 5 mM of Bi₂Fe₄O₉, TMB, and H₂O₂ respectively. In this study, the optimum
 383 concentrations were utilized to carry out the following experiments. The result in **Fig. S4D**
 384 demonstrated that pH values higher than 3.5 may cause the decomposition of H₂O₂ substrate
 385 into H₂O and O₂ molecules. Consequently, the rate of the formation of •OH radicals was
 386 decreased, and the distinct blue color-change was obtained only in an acidic condition.
 387 Therefore, the pH value of 3.5 was selected as the optimum pH that illustrated the blue-dark

388 color solution with the highest absorbance at 654 nm. Another effective factor was the
389 reaction temperature. In each case, the influence of the temperature on the peroxidase activity
390 of mimic-catalyst was investigated in a slightly acidic buffer (pH 3.5, 0.1 M). The catalytic
391 activity of the Bi₂Fe₄O₉ sharply increased when the temperature was raised from 10 to 45 °C,
392 and then decreased at temperatures higher than 45 °C. Therefore, the subsequent experiments
393 were performed at the optimal temperature of 45 °C (**Fig. S4E**). Moreover, incubation time
394 plays an important role in the decomposition of H₂O₂ and the accomplishment of the
395 oxidation reaction for which the selected optimal-time corresponds to 25 min (**Fig. S4F**). As
396 expected, the mimic-catalytic activity of Bi₂Fe₄O₉ depends on the concentration, pH,
397 temperature, and reaction-time, similar to other nanozymes reported in the literature.
398 According to the optimized values, it can be expected that Bi₂Fe₄O₉ nanozyme as a metal
399 oxide-type mimic catalyst can be applied for sensitive and accurate detection of dopamine.

400

401 3.4. Kinetic study of Bi₂Fe₄O₉ NPs and the determination of Michaelis-Menten constants

402 To explore the steady-state kinetic of Bi₂Fe₄O₉ as a peroxidase mimic nanozyme, various
403 concentrations of H₂O₂ and TMB as two different substrates were used to determine the
404 initial rate of H₂O₂ and TMB in acetate buffer (pH 3.5, 0.1 M) at 45 °C. In order to accurately
405 calculate the initial velocity rate, the Beer-Lambert Law was applied (**Eq. 5**).

$$406 \quad V = \frac{\Delta c}{\Delta t} = \frac{\frac{\Delta A}{\epsilon b}}{\Delta t}$$

407 (5)

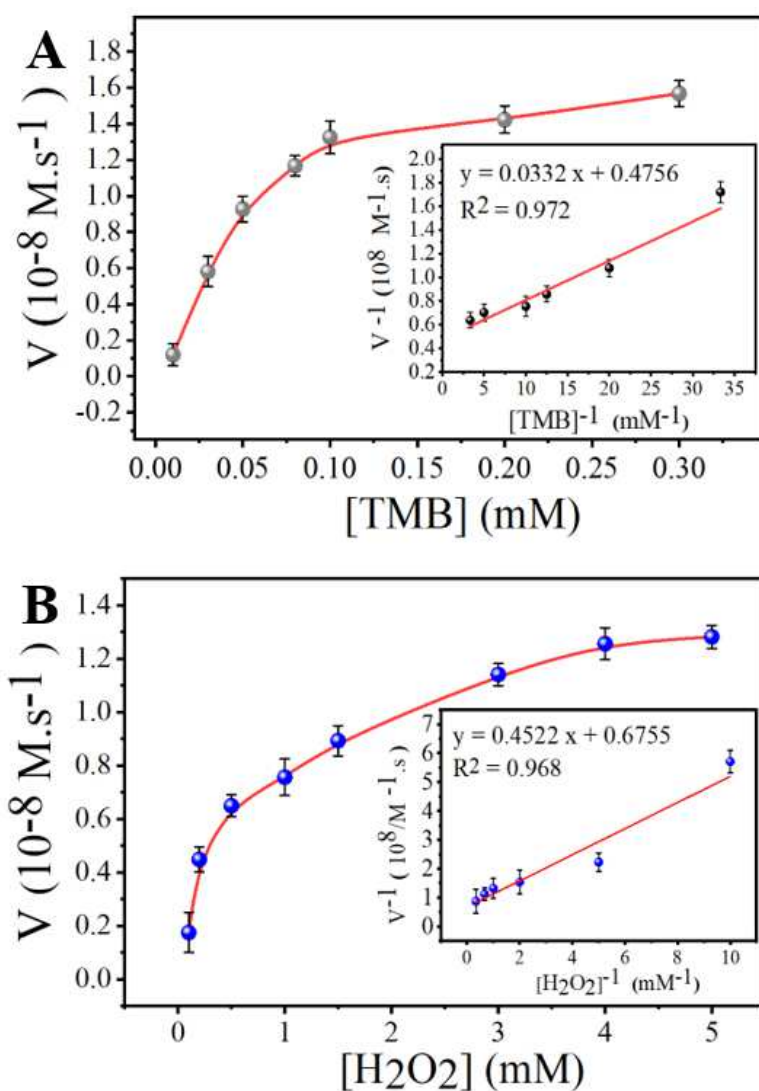
408 where A, b, ε, t and V represent respectively the absorbance at 654 nm, the optical path
409 length (1 cm), the molar absorptivity coefficient of oxTMB (39000 M⁻¹.cm⁻¹), the time (min),
410 and the reaction rate. In the time span of 0-30 min, **Fig S5 (A, B)** depicts the relationship
411 between the recorded UV-vis absorption spectra at 654 nm with the constant concentration of
412 one substrate (TMB or H₂O₂) and varying the concentration of the other substrate in the
413 reaction mixture. UV-vis absorption was dramatically increased and then reached a steady-
414 state level for both TMB (under the constant concentration of H₂O₂) and H₂O₂ (under the
415 constant concentration of TMB) substrates. And at this investigation time, the Michaelis-
416 Menten kinetic model fitted well the variation of the absorption process.

417 To determine the kinetic parameters, the Michaelis-Menten model is one of the earliest
418 descriptions and the best-known models to comprehensively investigate the value of
419 nanozyme kinetics activity. Michaelis-Menten kinetics of Bi₂Fe₄O₉ peroxidase-mimic

420 catalyst was determined by keeping constant the concentration of TMB or H₂O₂ as a targeted
421 substrate and varying the concentration of the other molecule in a time-scan mode,
422 simultaneously. Kinetic parameters (K_m and V_{max}) were calculated using the Lineweaver–
423 Burk plots of the double reciprocal of the Michaelis-Menten **Eq. 6**:

$$424 \frac{1}{v} = \frac{1}{[S]} \times \frac{K_m}{V_{max}} + \frac{1}{V_{max}} \quad (6)$$

425 where [S], v, V_{max}, and K_m refer to the substrate concentration, the initial reaction rate, the
426 maximum reaction rate, and Michaelis-Menten constant, respectively [6, 22, 60]. The steady-
427 state kinetic measurements were conducted for both TMB and H₂O₂ as enzyme substrates
428 (**Fig. 4A-B**). Under the optimized conditions, the Michaelis-Menten curves were generated
429 for TMB, at different concentrations of TMB (0.01-0.30 mM) and a fixed concentration of
430 H₂O₂ (5 mM), **Fig. 4A**, and also for H₂O₂ at various concentrations of H₂O₂ (0.1-5 mM) and
431 a constant concentration of TMB (0.30 mM), **Fig. 4B**. According to the obtained results, the
432 Michaelis-Menten constant (K_m) and maximum reaction rate (V_{max}) for H₂O₂/TMB/Bi₂Fe₄O₉
433 system were calculated and drawn via fitting the data into the Lineweaver Burk double
434 reciprocal plots (**Fig. 4A and B insets**).



435
 436 **Fig. 4.** Steady-state kinetic experiments of $\text{Bi}_2\text{Fe}_4\text{O}_9$ NPs at (A) different concentrations of
 437 TMB (0.01-0.30 mM) and fixed concentration of H_2O_2 (5 mM) substrates, and (B) varying
 438 concentrations of H_2O_2 (0.1-5 mM) and constant concentration of TMB (0.3 mM) substrates.
 439 Insets: the linear calibration curves for the determination of TMB and H_2O_2 . Reaction
 440 conditions: $\text{Bi}_2\text{Fe}_4\text{O}_9$ NPs (8 $\mu\text{g/mL}$), acetate buffer (pH 3.5, 0.1 M), $T=45^\circ\text{C}$, and incubation
 441 time=25 min. UV-vis measurements were repeated three times.

442
 443 **Table 1** summarizes the obtained enzyme kinetic parameters (K_m and V_{max}) in
 444 comparison to the horseradish peroxidase (HRP) enzyme and other nanomaterials reported in
 445 the literature. For TMB and H_2O_2 substrates in $\text{H}_2\text{O}_2/\text{TMB}/\text{Bi}_2\text{Fe}_4\text{O}_9$ system, the obtained
 446 constant K_m and V_{max} parameters equaled to 0.07 and 0.73 mM, and 2.17 and $1.56 (\times 10^{-8})$
 447 M.s^{-1} , respectively. In this context, the Michaelis-Menten constant (K_m) is an effective
 448 parameter to emphasize the affinity between the $\text{Bi}_2\text{Fe}_4\text{O}_9$ as an enzyme-like catalytic with

449 peroxidase substrate (TMB or H₂O₂). The lower value of K_m of Bi₂Fe₄O₉ in comparison to
 450 natural HRP and other nanozyme catalysts refer to its stronger affinity towards both TMB
 451 and H₂O₂ substrates. Besides, the lower K_m value of Bi₂Fe₄O₉ NPs for H₂O₂ means that the
 452 higher catalytic response of Bi₂Fe₄O₉ NPs was obtained using a small concentration of H₂O₂
 453 substrate. This means that the decomposition of H₂O₂ into •OH radical can be accelerated to
 454 oxidase TMB molecules. According to the obtained K_m and V_{max} constants, Bi₂Fe₄O₉ features
 455 a good affinity towards TMB and H₂O₂ for peroxidase-mimic activity.

456

457 **Table 1**

458 Comparison of the steady-state kinetic parameters (Michaelis-Menten constant (K_m) and
 459 maximum velocity (V_m) of H₂O₂ and TMB substrates with previously reported materials.

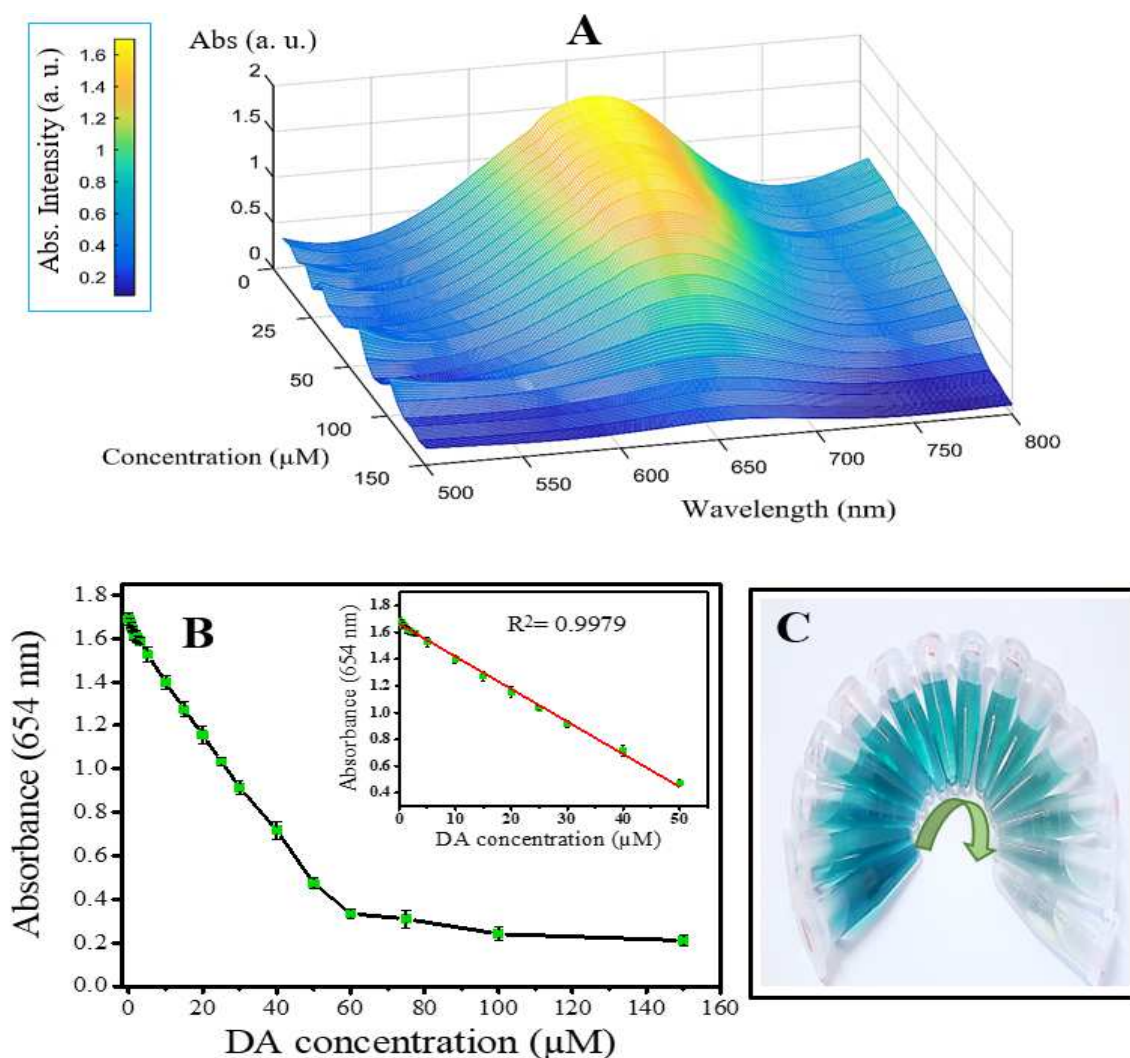
Catalysts	Substrates	K _m (mM)	V _m (10 ⁻⁸ M.s ⁻¹)	Ref.
HRP	H ₂ O ₂	3.70	8.71	[24]
HRP	TMB	0.43	10.00	[24]
CuFe ₂ O ₄ /Cu ₉ S ₈ /PPy	H ₂ O ₂	23.83	9.82	[47]
CuFe ₂ O ₄ /Cu ₉ S ₈ /PPy	TMB	0.13	6.97	[47]
Co ₃ O ₄ gilly-flower like	H ₂ O ₂	245.00	28.50	[61]
Co ₃ O ₄ gilly-flower like	TMB	0.12	33.20	[61]
MoS ₂ /PPy	H ₂ O ₂	12.80	15.10	[62]
MoS ₂ /PPy	TMB	0.41	47.40	[62]
Bi ₂ Fe ₄ O ₉	H ₂ O ₂	0.73	1.56	This work
Bi ₂ Fe ₄ O ₉	TMB	0.07	2.17	This work

460

461 *3.5. Colorimetric sensing of dopamine in the presence of Bi₂Fe₄O₉ nanozyme*

462 In order to demonstrate the acceptable enzyme-mimetic property of Bi₂Fe₄O₉ nanozyme,
 463 the optimized H₂O₂/TMB/Bi₂Fe₄O₉ system was applied as an indirect platform to sense
 464 dopamine. As displayed in **Fig. 5A-B**, the presence of dopamine molecule with an effective
 465 inhibiting role, prevents the formation ox-TMB under optimum conditions. A point of fact
 466 during the increase of dopamine concentration is the gradual vanishing of the dark-blue color
 467 and the decreased number of ox-TMB molecules (**Fig. 5C**). Therefore, the presence of

468 dopamine effectively prohibited the production of ox-TMB molecules. The color changes of
469 TMB solutions were easily observable by naked eyes and the variation of the UV-vis spectra
470 was recorded at 654 nm. This phenomenon clearly indicated the competition between
471 dopamine and TMB molecules to capture $\cdot\text{OH}$ generated in the catalytic decomposition of
472 H_2O_2 molecules. The notable decrease of accessible $\cdot\text{OH}$ radicals may be the result of
473 phenolic ring oxidation in dopamine molecules [1, 60]. Generally, dopamine oxidation was
474 accelerated using $\text{Bi}_2\text{Fe}_4\text{O}_9$ nanozyme to produce dopamine o-quinone (DOQ). The defined
475 system outlines a simple colorimetric platform for dopamine sensing that is based on the
476 oxidation of dopamine by utilizing H_2O_2 molecules in presence of $\text{Bi}_2\text{Fe}_4\text{O}_9$ nanozyme and
477 TMB substrate.
478



479
480 **Fig. 5.** UV-vis absorption spectra (A) and absorbance at 654 nm (B) of TMB solutions in
481 presence of $\text{Bi}_2\text{Fe}_4\text{O}_9$ nanozyme and various DA concentrations (0-150 μM). Inset: The linear
482 calibration curve in the lower concentration range of DA ($R^2=0.9979$). Photographs of the

483 color-changes during TMB oxidation in presence of different dopamine concentrations (C)
484 (from left to right arrow: increasing the concentration of dopamine). Reaction conditions:
485 Bi₂Fe₄O₉ NPs (8 μg/mL), TMB (0.3 mM), H₂O₂ (5 mM), acetate buffer (pH 3.5, 0.1 M),
486 T=45 °C, and incubation time=25 min. The measurements were performed in triplicates.

487

488 An elevation of dopamine concentration from 0 to 150 μM led to a decrease in
489 absorbance intensity of ox-TMB at 654 nm. The color tonality faded from deep-blue to
490 colorless, indicating a decrease in the oxidation rate of TMB oxidation and enhanced
491 formation of dopamine o-quinone molecule (**Fig. 5C**). A good linear range of added
492 dopamine (from 0.15 to 50 μM) to TMB/H₂O₂/Bi₂Fe₄O₉ system was obtained by applying the
493 equation $A = -0.024 [\text{dopamine } (\mu\text{M})] + 1.663$ ($R^2=0.9979$). In addition, the limit of detection
494 (LOD) was determined to be 51 nM at S/N=3, where S and N represent the signal and noise,
495 respectively.

496 **Table 2** lists the analytical merits of the developed Bi₂Fe₄O₉ nanozyme sensor compared
497 to different nanoparticles using various approaches such as electrochemistry [17, 18],
498 electrochemiluminescence [16], fluorescence spectroscopy [13], and colorimetric assays [3,
499 23]. The value of the LOD of our colorimetric-method by using Bi₂Fe₄O₉ nanozyme is lower
500 than previously reported ones. The above results indicate that this designed colorimetric
501 sensor as a simple, facile, and reproducible assay has a high sensitivity to detect dopamine
502 molecules.

503

504

505

506

507

508

509

510

511

512

513

514

515

516

517
518
519
520

Table 2

Method	Sensor	Linear range (μM)	LOD ¹ (μM)	Ref.
Electrochemistry	rGO/TiO ₂	2-60	0.60	[17]
Electrochemistry	CAuNE	1-100	5.83	[18]
ECL ²	CdSeTe/ZnS QDs	3.75-450	0.10	[16]
Fluorescence	BSA-CuNCs	0.50-50	0.28	[13]
Colorimetric	LaCoO ₃	0.50-20	0.19	[3]
Colorimetric	Co ₃ O ₄ @NiO	1-1000	1.21	[60]
Colorimetric	CuS/rGO	2-100	0.48	[63]
Colorimetric	Ag NPs	3.20-20	1.20	[64]
Colorimetric	CuFe ₂ O ₄ /Cu ₉ S ₈ /PPy	2-20	1.00	[35]
Colorimetric	h-CuS NCs	2-150	1.67	[65]
Colorimetric	NiCo ₂ S ₄ -rGO	0.50-100	0.42	[23]
Colorimetric	Bi ₂ Fe ₄ O ₉	0.15-50	0.05	This work

521 Comparison of different analytical methods for quantitative analysis of dopamine.

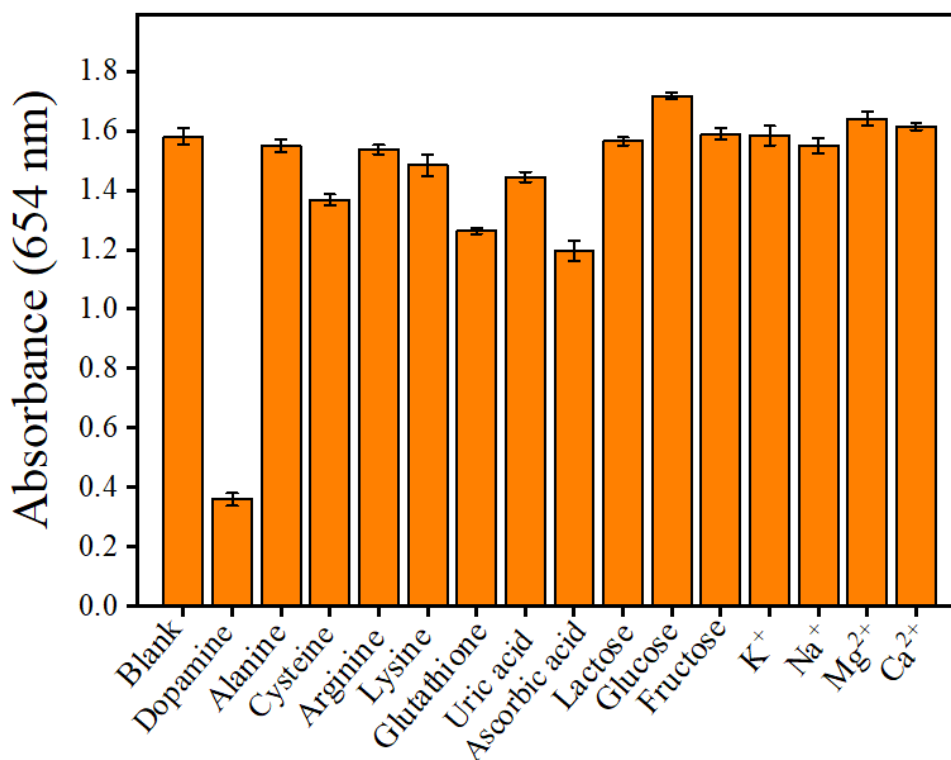
522 ¹ Limit of detection (LOD)

523 ² Electrochemiluminescence (ECL)

524

525 3.6. Selectivity of Bi₂Fe₄O₉ nanozyme-sensor toward dopamine detection

526 Under the optimized conditions, the selectivity of the proposed Bi₂Fe₄O₉ nanozyme was
527 investigated in the presence of different molecules such as alanine (Ala), cysteine (Cys),
528 arginine (Arg), lysine (Lys), glutathione (GSH), uric acid (UA), ascorbic acid (AA), lactose
529 (Lac), glucose (Glu), fructose (Fru), K⁺, Na⁺, Mg²⁺, and Ca²⁺, with the concentration two
530 times higher (100 μM) than the optimized concentration of dopamine. The reduction of UV–
531 vis absorbance intensity in H₂O₂/TMB/Bi₂Fe₄O₉/interfering system was compared to control
532 condition (**Fig. 6**). The excellent inhibition role of dopamine in comparison to other
533 molecules (at higher concentration) indicates that ox-TMB product could not easily be
534 generated in the dopamine-containing system.



535

536 **Fig. 6.** Absorption at 654 nm of oxTMB in the presence of different interfering molecules at a
 537 concentration of 100 μ M (2 times higher than the concentration of DA); Reaction conditions:
 538 Bi₂Fe₄O₉ NPs (8 μ g/mL), H₂O₂ (5 mM), TMB (0.3 mM), acetate buffer (0.1 M, pH 3.5),
 539 T=45 °C, and incubation time=25 min. The measurements were performed in triplicates.

540

541 Dopamine is a strong free radical scavenger and has a potent hydrogen-donating activity.
 542 As presented in **Fig. 6**, the excellent inhibition role of dopamine in comparison to the applied
 543 interference molecules is obviously reflected from its higher tendency to capture hydroxyl
 544 radicals (\cdot OH) in the acidic medium and prohibit the oxidation of TMB molecules. The
 545 higher quenching ability of dopamine is related to its specific chemical structure. Dopamine
 546 features several H atoms on its aromatic ring responsible for increasing the electron density,
 547 mobility, and also the propensity to capture \cdot OH radicals. During the reaction with the
 548 reactive oxygen species (ROS) like \cdot OH radical, dopamine is able to produce several
 549 derivatives (**Scheme S2 B-D**). As indicated in **Scheme S2**, three initial-hydroxylated
 550 products of dopamine are generated during the reaction with \cdot OH radical, namely 2-
 551 hydroxydopamine (2-OHDA), 5-hydroxydopamine (5-OHDA), and 6-hydroxydopamine (6-
 552 OHDA). All three ring-monohydroxylated dopamine molecules as reactive species could
 553 inhibit the oxidation of TMB molecules to oxTMB [1]. Another effective factor of dopamine
 554 for inhibiting TMB oxidation is associated with the presence of its ethyl-amine group. The

555 amine group in the side chain of the dopamine phenolic ring, as a suitable electron-donor
556 group, helps to accelerate electron transfer to enhance the interaction among H atoms on
557 aromatic rings of dopamine with $\cdot\text{OH}$ radicals. This result means that dopamine has higher
558 quenching ability of $\cdot\text{OH}$ radicals compared to ascorbic acid and uric acid [5, 66]. This
559 oxidation process indicated that the designed colorimetric probe owns a good selectivity and
560 could play an important role in the low detection of dopamine in aqueous media.

561

562 *3.7. Reproducibility of $\text{Bi}_2\text{Fe}_4\text{O}_9$ nanoparticles*

563 To investigate the nanozyme efficiency, a fresh sample of $\text{Bi}_2\text{Fe}_4\text{O}_9$ NPs (8 $\mu\text{g}/\text{mL}$), TMB
564 (0.3 mM), and H_2O_2 (5 mM) in acetate buffer (pH 3.5, 0.1 M) at 45 $^\circ\text{C}$ was slightly shaken
565 for 25 min. The final volume of the solution was 1.5 mL. For the repeated cycle purpose,
566 $\text{H}_2\text{O}_2/\text{TMB}/\text{Bi}_2\text{Fe}_4\text{O}_9$ reaction mixture was centrifuged at 10,000 rpm for 7 min and rinsed
567 with deionized water at 25 $^\circ\text{C}$ and then the precipitate was added to $\text{H}_2\text{O}_2/\text{TMB}$ solution
568 under the obtained optimal conditions. The relative activity versus response cycle is depicted
569 in **Fig. S6**. The catalytic stability of $\text{Bi}_2\text{Fe}_4\text{O}_9$ after every catalytic cycle, compared with the
570 original activity, was slightly reduced. After the fourth independent cycle, the primary
571 absorbance intensity of the fresh mixture was decreased from 100% to 93%. The result
572 proved that $\text{Bi}_2\text{Fe}_4\text{O}_9$ NPs exhibit a good enzyme-like catalytic activity, stability, and
573 reproducibility.

574

575 *3.8. Detection of dopamine in real samples*

576 To evaluate the practical applicability of the proposed $\text{Bi}_2\text{Fe}_4\text{O}_9$ NPs as an efficient
577 enzyme-like catalyst, we examined dopamine determination in fetal bovine serum (FBS), and
578 horse serum (HS) samples. It should be noted that FBS and HS samples before adding the
579 reagents were diluted 1000 times with buffer phosphate saline (PBS 0.1 mM, pH 7.4). Using
580 the optimized conditions ($\text{Bi}_2\text{Fe}_4\text{O}_9$ NPs (8 mg/mL), H_2O_2 (5 mM), TMB (0.3 mM), pH= 3.5,
581 incubation time=25 min, and T=45 $^\circ\text{C}$), different concentrations of dopamine (1, 5, and 10
582 μM) were spiked into diluted FBS 1 (Sigma-Aldrich), FBS 2 (Fisher Scientific), and HS
583 (Fisher Scientific) solutions.

584 Moreover, the recovery values and the content of dopamine in real samples were
585 calculated using the obtained calibration curve in **Fig. 5** and the recorded UV-vis absorption
586 spectra at 654 nm for every real sample (FBS 1, FBS 2, and HS). The result of percentage
587 recovery ($[\text{dopamine}]_{\text{found}}/[\text{dopamine}]_{\text{added}} \times 100$) and relative standard deviation (RSD %) are
588 listed in **Table 3**. The relative recoveries of dopamine concentration in FBS (1 and 2) and HS

589 samples were respectively in the ranges of 96.18–118.12% and 97.61–104.92%. It should be
 590 noted that to reduce the stochastic error effect, UV-vis absorbance values were recorded
 591 three-times for each experimental condition. The results revealed that this colorimetric
 592 method, as a feasible and reliable approach, can be applied to determine dopamine in
 593 different real samples.

594

595 **Table 3**

596 Sensing of DA in fetal bovine serum (FBS 1 and 2), and horse serum (HS) samples (n = 3).

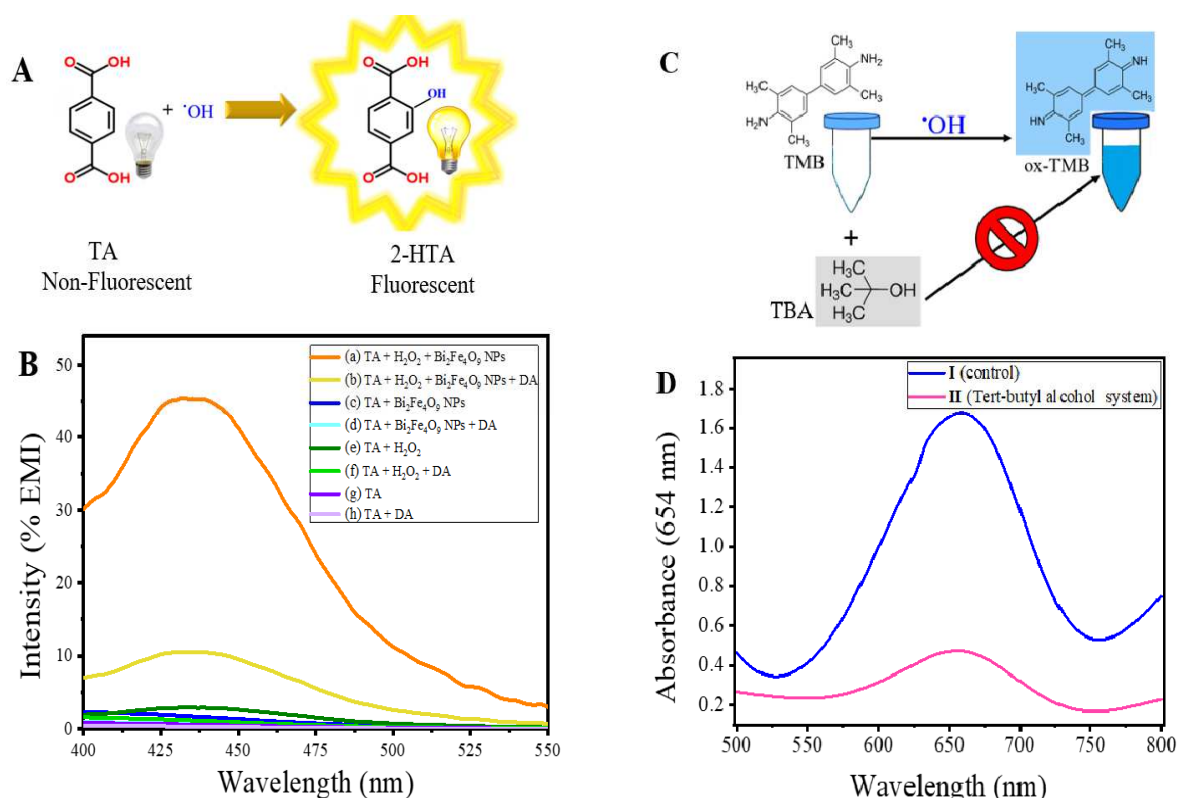
Samples	DA added (μM)	DA founded (μM)	Recovery (%)	RSD (%)
FBS 1	1.00	1.02	101.78	0.39
	5.00	5.35	106.95	0.64
	10.00	9.62	96.18	1.76
FBS 2	1.00	1.16	116.22	1.66
	5.00	5.40	108.02	0.39
	10.00	11.81	118.12	3.81
HS	1.00	0.97	97.61	1.42
	5.00	5.10	102.04	0.80
	10.00	10.49	104.92	3.27

597

598 3.9. The investigation of the mimic-enzyme catalytic mechanism to produce hydroxyl radicals 599 ($\cdot\text{OH}$)

600 To confirm the peroxidase-like mechanism of $\text{Bi}_2\text{Fe}_4\text{O}_9$ NPs, terephthalic acid (TA)
 601 molecule was selected as a fluorescence probe. As indicated in **Fig. 7**, TA can react with $\cdot\text{OH}$
 602 radicals to yield 2-hydroxyterephthalic acid (HTA) molecule, displaying an intense
 603 fluorescence signal [6, 67-69]. The general oxidation reaction of the TA molecule is depicted
 604 in the following **Fig. 7A**. All the solutions (**Fig. 7B**) were prepared in acetate buffer (pH 3.5,
 605 0.1 M) and the total value was 1.5 mL. As presented in **Fig. 7B (g, e, and c)**, terephthalic acid
 606 (TA) did not show an obvious emission peak in the absence of H_2O_2 , the presence of H_2O_2
 607 alone, and $\text{Bi}_2\text{Fe}_4\text{O}_9$ NPs alone. It could be clearly seen, in **Fig. 7B (a)**, that the introduction
 608 of $\text{Bi}_2\text{Fe}_4\text{O}_9$ nanozyme to TA/ H_2O_2 mixture led to the appearance of fluorescence emission
 609 with a maximum peak at around 435 nm under optimum experimental conditions, which is a
 610 strong indication that TA was converted into HTA molecules. The fluorescence curves
 611 indicated that the formation of HTA molecules was highly related to the presence of both

612 H_2O_2 substrate and $\text{Bi}_2\text{Fe}_4\text{O}_9$ nanozyme in the reaction mixture ($\text{H}_2\text{O}_2/\text{Bi}_2\text{Fe}_4\text{O}_9/\text{TA}$). In the
 613 presence of dopamine, the fluorescence intensity of obtained HTA was dramatically
 614 decreased, which proved the competitive role of dopamine compared to TA for grasping the
 615 hydroxide radicals (**Fig. 7B (b), orange curve**). The fluorescence intensity related to HTA
 616 molecules in each of the eight solutions was recorded at 435 nm. The transformation of TA
 617 into fluorescent (HTA) molecules was accelerated in the presence of $\text{Bi}_2\text{Fe}_4\text{O}_9$ nanozyme
 618 through the decomposition of H_2O_2 molecules into hydroxyl radicals ($\cdot\text{OH}$).



620
 621 **Fig. 7.** (A) The possible mechanism of reaction of terephthalic acid (TA) with hydroxyl
 622 radicals. (B) Fluorescence spectra using TA as a fluorescent probe ($\lambda_{ex}=315$ nm), Reaction
 623 experimental conditions: (a) H_2O_2 (5 mM) + $\text{Bi}_2\text{Fe}_4\text{O}_9$ NPs (8 $\mu\text{g}/\text{mL}$), (b) H_2O_2 (5 mM) +
 624 $\text{Bi}_2\text{Fe}_4\text{O}_9$ NPs (8 $\mu\text{g}/\text{mL}$) + dopamine (50 μM), (c) $\text{Bi}_2\text{Fe}_4\text{O}_9$ NPs (8 $\mu\text{g}/\text{mL}$), (d) $\text{Bi}_2\text{Fe}_4\text{O}_9$
 625 NPs (8 $\mu\text{g}/\text{mL}$) + dopamine (50 μM), (e) H_2O_2 (5 mM), (f) H_2O_2 (5 mM) + dopamine (50
 626 μM), (g) only TA (0.2 mM), and (h) TA (0.2 mM) + dopamine (50 μM) in acetate buffer (pH
 627 3.5, 0.1 M) and all solutions were incubated for 25 min at 45 $^\circ\text{C}$. (C) The proposed
 628 mechanism of effect of *tert*-butyl alcohol (TBA) on the peroxidase-mimic catalytic activity of
 629 $\text{Bi}_2\text{Fe}_4\text{O}_9$ NPs. (D) UV-vis spectra using TBA as an electron scavenger, Reaction
 630 experimental conditions: $\text{Bi}_2\text{Fe}_4\text{O}_9$ NPs (8 $\mu\text{g}/\text{mL}$), TMB (0.3 mM), H_2O_2 (5 mM), acetate
 631 buffer (pH 3.5, 0.1 M), TBA (0.5 mM), T=45 $^\circ\text{C}$, and incubation time=25 min.

632 In addition, to confirm the role of $\cdot\text{OH}$ radicals in the reaction mechanism, *tert*-butanol
633 alcohol (TBA) was used as $\cdot\text{OH}$ radical scavenger molecule (rate constant = $6.2 \times 10^8 \text{ dm}^3$
634 $\text{mol}^{-1} \text{ s}^{-1}$). The presence of TBA obviously prevented the oxidation of TMB molecules and
635 simultaneously produced $(\cdot(\text{CH}_3)_3\text{O})$ radicals [7, 70]. As mentioned above, TBA can directly
636 quench reactive oxygen species (ROS) as hydroxyl radicals (**Fig. 7C-D**). The comparison of
637 the UV-vis absorption spectra of the $\text{H}_2\text{O}_2/\text{TMB}/\text{Bi}_2\text{Fe}_4\text{O}_9$ (**Fig. 7D, blue curve**) and
638 $\text{H}_2\text{O}_2/\text{TMB}/\text{Bi}_2\text{Fe}_4\text{O}_9/\text{TBA}$ (**Fig. 7D, pink curve**) systems illustrated an obvious absorption
639 peak in the UV-vis range whose intensity was significantly decreased in the presence of
640 TBA. These phenomena prove that the hydroxyl radicals play an important role in the
641 oxidation of TMB substrate and the charge transfer between Fe (II) to Fe (III) ions in the
642 Fenton-like cycle of $\text{Bi}_2\text{Fe}_4\text{O}_9$ nanozyme.

643

644 **4. Conclusion**

645 In summary, dopamine (DA) as a neurotransmitter plays a number of key roles in
646 humans and animals. Therefore, the control and monitoring of the amount of dopamine is
647 necessary to prevent disease conditions. In this work, we report, for the first time, a new
648 colorimetric sensor using $\text{Bi}_2\text{Fe}_4\text{O}_9$ nanoparticles with peroxidase-mimic catalytic activity.
649 The metal-based bimetallic $\text{Bi}_2\text{Fe}_4\text{O}_9$ NPs were prepared by a hydrothermal method that is a
650 facile and low-cost approach. $\text{Bi}_2\text{Fe}_4\text{O}_9$ enzyme mimic features high water-solubility and
651 good stability. On the basis of the outstanding catalytic activity of $\text{Bi}_2\text{Fe}_4\text{O}_9$ in the presence of
652 TMB and H_2O_2 , a colorimetric sensing platform was developed and exhibited an accurate,
653 highly sensitive, and selective detection of dopamine at a nanomolar level. This colorimetric
654 probe achieved a detection limit and linear concentration range of 51 nM and 0.15-50 μM for
655 dopamine, respectively. The developed sensor outperforms the already reported nanozymes
656 in literature [3, 35, 63-65]. Under optimized experimental conditions, Michaelis-Menten
657 kinetics analysis of the oxidation state of TMB substrate, in $\text{H}_2\text{O}_2/\text{TMB}/\text{Bi}_2\text{Fe}_4\text{O}_9$ system,
658 achieved V_{max} and K_{m} values of $2.17 \times 10^{-8} \text{ M}\cdot\text{s}^{-1}$ and 0.07 mM, respectively. To gain a better
659 understanding of the reaction mechanism, we examined the effect of hydroxyl ($\cdot\text{OH}$) radicals
660 as important reactive oxygen species to oxidase dopamine molecules in the
661 $\text{H}_2\text{O}_2/\text{TMB}/\text{Bi}_2\text{Fe}_4\text{O}_9/\text{DA}$ colorimetric-system using terephthalic acid (TA) and *tert*-butyl
662 alcohol (TBA) probes. This spectroscopic method for evaluation of $\cdot\text{OH}$ radicals is a simple,
663 inexpensive, and reliable approach. In addition, the potential application of $\text{Bi}_2\text{Fe}_4\text{O}_9$ as a
664 peroxidase-mimic catalyst to accurately detect dopamine concentration in fetal bovine serum

665 (FBS) and horse serum (HS) samples was demonstrated. Taken together the results of the
666 present study highlight the potential application of nanostructured bismuth ferrite ($\text{Bi}_2\text{Fe}_4\text{O}_9$)
667 in the diagnosis of dopamine-related diseases. Future work will introduce the investigation of
668 dopamine in real samples by using lateral-flow test strips coupled with smartphones. These
669 studies will open new perspectives for early detection and treatment of different types of drug
670 addiction and neurological related diseases.

671

672 **CRedit authorship contribution statement**

673 **Mehri Razavi:** Investigation, Methodology, Validation, Visualization, Formal analysis,
674 Writing-original draft. **Alexandre Barras:** Investigation, Methodology. **Majdid Ifires:**
675 Resources. **Abir Swaidan:** Resource. **Maryam Khoshkam:** Investigation. **Sabine**
676 **Szunerits:** Investigation. **Mohsen Kompany-Zareh:** Writing-reviewing and editing. **Rabah**
677 **Boukherroub:** Supervision, Conceptualization, Writing-review & editing, Funding
678 acquisition, Project administration.

679

680 **Declaration of Competing Interest**

681 The authors declare that they have no known competing financial interests or personal
682 relationships that could have appeared to influence the work reported in this paper.

683

684 **Acknowledgments**

685 The authors wish to thank the Centre National de la Recherche Scientifique (CNRS), the
686 University of Lille, the region Hauts-de-France, the CPER “Photonics for Society”, and the
687 Institute for Advanced Studies in Basic Sciences (IASBS) in Iran for supporting this study.

688

689

690

691

692

693

694 **References**

- 695 [1] A. Slivka, G. Cohen, Hydroxyl radical attack on dopamine, *J. Biol. Chem.* 260 (1985)
696 15466-15472.
- 697 [2] J. Liu, L. Yuan, X. Dong, Recent advances in analytical techniques for the determination
698 of dopamine, *Int. J. Chem. Stud.* 3 (2015) 39-45.
- 699 [3] K. Wang, J. Song, X. Duan, J. Mu, Y. Wang, Perovskite LaCoO₃ nanoparticles as enzyme
700 mimetics: their catalytic properties, mechanism and application in dopamine biosensing, *New*
701 *J. Chem.* 41 (2017) 8554-8560.
- 702 [4] P.A. Rasheed, J.-S. Lee, Recent advances in optical detection of dopamine using
703 nanomaterials, *Microchim. Acta* 184 (2017) 1239-1266.
- 704 [5] G.-C. Yen, C.-L. Hsieh, Antioxidant effects of dopamine and related compounds, *Biosci.*
705 *Biotechnol. Biochem.* 61 (1997) 1646-1649.
- 706 [6] M.N. Ivanova, E.D. Grayfer, E.E. Plotnikova, L.S. Kibis, G. Darabdhara, P.K. Boruah,
707 M.R. Das, V.E. Fedorov, Pt-decorated boron nitride nanosheets as artificial nanozyme for
708 detection of dopamine, *ACS Appl. Mater. Interfaces* 11 (2019) 22102-22112.
- 709 [7] A. Swaidan, A. Barras, A. Addad, J.-F. Tahon, J. Toufaily, T. Hamieh, S. Szunerits, R.
710 Boukherroub, Colorimetric sensing of dopamine in beef meat using copper sulfide
711 encapsulated within bovine serum albumin functionalized with copper phosphate (CuS-BSA-
712 Cu₃(PO₄)₂) nanoparticles, *J. Colloid Interface Sci.* 582 (2021) 732-740.
- 713 [8] S. Rostami, A. Mehdinia, A. Jabbari, Intrinsic peroxidase-like activity of graphene
714 nanoribbons for label-free colorimetric detection of dopamine, *Mater. Sci. Eng. C* 114 (2020)
715 111034-111044.
- 716 [9] G.E. De Benedetto, D. Fico, A. Pennetta, C. Malitesta, G. Nicolardi, D.D. Lofrumento, F.
717 De Nuccio, V. La Pesa, A rapid and simple method for the determination of 3, 4-
718 dihydroxyphenylacetic acid, norepinephrine, dopamine, and serotonin in mouse brain
719 homogenate by HPLC with fluorimetric detection, *J. Pharm. Biomed. Anal.* 98 (2014) 266-
720 270.
- 721 [10] H. Fang, M.L. Pajski, A.E. Ross, B.J. Venton, Quantitation of dopamine, serotonin and
722 adenosine content in a tissue punch from a brain slice using capillary electrophoresis with
723 fast-scan cyclic voltammetry detection, *Anal. Methods* 5 (2013) 2704-2711.
- 724 [11] Y. Dong, H. Chen, Y. Chen, Y. Hui, X. Chen, Z. Hu, Separation and determination of
725 epinephrine and dopamine in traditional Chinese medicines by micellar electrokinetic
726 capillary chromatography with laser induced fluorescence detection, *J. Sep. Sci.* 29 (2006)
727 2049-2055.
- 728 [12] S.J. Park, S.H. Lee, H. Yang, C.S. Park, C.-S. Lee, O.S. Kwon, T.H. Park, J. Jang,
729 Human dopamine receptor-conjugated multidimensional conducting polymer nanofiber
730 membrane for dopamine detection, *ACS Appl. Mater. Interfaces* 8 (2016) 28897-28903.
- 731 [13] Z. Miao, W. Hou, M. Liu, Y. Zhang, S. Yao, BSA capped bi-functional fluorescent Cu
732 nanoclusters as pH sensor and selective detection of dopamine, *New J. Chem.* 42 (2018)
733 1446-1456.
- 734 [14] B. Xu, Y. Su, L. Li, R. Liu, Y. Lv, Thiol-functionalized single-layered MoS₂ nanosheet
735 as a photoluminescence sensing platform via charge transfer for dopamine detection,
736 *Sens. Actuators B* 246 (2017) 380-388.
- 737 [15] W.Z.W. Ismail, G. Liu, K. Zhang, E.M. Goldys, J.M. Dawes, Dopamine sensing and
738 measurement using threshold and spectral measurements in random lasers, *Opt. Express* 24
739 (2016) A85-A91.
- 740 [16] A.J. Stewart, J. Hendry, L. Dennany, Whole blood electrochemiluminescent detection of
741 dopamine, *Anal. Chem.* 87 (2015) 11847-11853.

742 [17] G.T.S. How, A. Pandikumar, H.N. Ming, L.H. Ngee, Highly exposed {001} facets of
743 titanium dioxide modified with reduced graphene oxide for dopamine sensing, *Sci. Rep.* 4
744 (2014) 1-8.

745 [18] D.-S. Kim, E.-S. Kang, S. Baek, S.-S. Choo, Y.-H. Chung, D. Lee, J. Min, T.-H. Kim,
746 Electrochemical detection of dopamine using periodic cylindrical gold nanoelectrode arrays,
747 *Sci. Rep.* 8 (2018) 1-10.

748 [19] H. Wei, E. Wang, Nanomaterials with enzyme-like characteristics (nanozymes): next-
749 generation artificial enzymes, *Chem. Soc. Rev.* 42 (2013) 6060-6093.

750 [20] Y. Lin, J. Ren, X. Qu, Catalytically active nanomaterials: a promising candidate for
751 artificial enzymes, *Acc. Chem. Res.* 47 (2014) 1097-1105.

752 [21] N. Chaibakhsh, Z. Moradi-Shoeili, Enzyme mimetic activities of spinel substituted
753 nanoferrites (MFe₂O₄): A review of synthesis, mechanism and potential applications, *Mater.*
754 *Sci. Eng. C* 99 (2019) 1424-1447.

755 [22] A. Swaidan, A. Addad, J.-F. Tahon, A. Barras, J. Toufaily, T. Hamieh, S. Szunerits, R.
756 Boukherroub, Ultrasmall CuS-BSA-Cu₃(PO₄)₂ nanozyme for highly efficient colorimetric
757 sensing of H₂O₂ and glucose in contact lens care solutions and human serum, *Anal. Chim.*
758 *Acta* 1109 (2020) 78-89.

759 [23] Y. Wang, L. Yang, Y. Liu, Q. Zhao, F. Ding, P. Zou, H. Rao, X. Wang, Colorimetric
760 determination of dopamine by exploiting the enhanced oxidase mimicking activity of
761 hierarchical NiCo₂S₄-rGO composites, *Microchim. Acta* 185 (2018) 1-9.

762 [24] L. Gao, J. Zhuang, L. Nie, J. Zhang, Y. Zhang, N. Gu, T. Wang, J. Feng, D. Yang, S.
763 Perrett, Intrinsic peroxidase-like activity of ferromagnetic nanoparticles, *Nat. Nanotechnol.* 2
764 (2007) 577-583.

765 [25] R. Awasthi, B. Das, Effect of temperature on physical properties of Bi₂Fe₄O₉
766 polycrystalline materials, *J. Aust. Ceram. Soc.* 56 (2020) 243-250.

767 [26] Z.-T. Hu, S.K. Lua, X. Yan, T.-T. Lim, Nanostructured hexahedron of bismuth ferrite
768 clusters: delicate synthesis processes and an efficient multiplex catalyst for organic pollutant
769 degradation, *RSC Adv.* 5 (2015) 86891-86900.

770 [27] B. Li, C. Lai, G. Zeng, L. Qin, H. Yi, D. Huang, C. Zhou, X. Liu, M. Cheng, P. Xu,
771 Facile hydrothermal synthesis of Z-scheme Bi₂Fe₄O₉/Bi₂WO₆ heterojunction photocatalyst
772 with enhanced visible light photocatalytic activity, *ACS Appl. Mater. Interfaces* 10 (2018)
773 18824-18836.

774 [28] A. Poghossian, H. Abovian, P. Avakian, S. Mkrtchian, V. Haroutunian, Bismuth ferrites:
775 New materials for semiconductor gas sensors, *Sens. Actuators B* 4 (1991) 545-549.

776 [29] N. Zakharchenko, Catalytic properties of the Fe₂O₃-Bi₂O₃ system in ammonia oxidation
777 to nitrogen oxides, *Kinet. Catal.* 43 (2002) 95-98.

778 [30] Z.-T. Hu, J. Liu, X. Yan, W.-D. Oh, T.-T. Lim, Low-temperature synthesis of graphene/
779 Bi₂Fe₄O₉ composite for synergistic adsorption-photocatalytic degradation of hydrophobic
780 pollutant under solar irradiation, *Chem. Eng. J.* 262 (2015) 1022-1032.

781 [31] M. Kong, H. Song, F. Li, D. Dai, H. Gao, Facile synthesis of Bi₂Fe₄O₉ nanoplate and its
782 application as a novel adsorbent for Cu (II) removal, *J. Environ. Chem. Eng.* 5 (2017) 69-78.

783 [32] A. Roy, R. Gupta, A. Garg, Multiferroic memories, *Adv. Condens. Matter Phys.* 2012
784 (2012) 1-12.

785 [33] J. Scott, Multiferroic memories, *Nat. Mater.* 6 (2007) 256-257.

786 [34] J.T. Han, Y.H. Huang, X.J. Wu, C.L. Wu, W. Wei, B. Peng, W. Huang, J.B.
787 Goodenough, Tunable synthesis of bismuth ferrites with various morphologies, *Adv. Mater.*
788 18 (2006) 2145-2148.

789 [35] Z. Yang, F. Ma, Y. Zhu, S. Chen, C. Wang, X. Lu, A facile synthesis of CuFe₂O
790 ₄/Cu₉S₈/PPy ternary nanotubes as peroxidase mimics for the sensitive colorimetric detection
791 of H₂O₂ and dopamine, *Dalton Trans.* 46 (2017) 11171-11179.

792 [36] Q. Chen, C. Liang, X. Zhang, Y. Huang, High oxidase-mimic activity of Fe
793 nanoparticles embedded in an N-rich porous carbon and their application for sensing of
794 dopamine, *Talanta* 182 (2018) 476-483.

795 [37] X. Wang, M. Zhao, Y. Song, Q. Liu, Y. Zhang, Y. Zhuang, S. Chen, Synthesis of
796 $\text{ZnFe}_2\text{O}_4/\text{ZnO}$ heterostructures decorated three-dimensional graphene foam as peroxidase
797 mimetics for colorimetric assay of hydroquinone, *Sens. Actuators B* 283 (2019) 130-137.

798 [38] Y. Xing, M. Chen, Y. Zhao, J. Xu, X. Hou, Triple-enzyme mimetic activity of $\text{Fe}_3\text{O}_4@$
799 $\text{C}@\text{MnO}_2$ composites derived from metal-organic frameworks and their application to
800 colorimetric biosensing of dopamine, *Microchim. Acta* 189 (2022) 1-10.

801 [40] J. Yu, D. Ma, L. Mei, Q. Gao, W. Yin, X. Zhang, L. Yan, Z. Gu, X. Ma, Y. Zhao,
802 Peroxidase-like activity of MoS_2 nanoflakes with different modifications and their application
803 for H_2O_2 and glucose detection, *J. Mater. Chem. B* 6 (2018) 487-498.

804 [41] F. Yu, Y. Huang, A.J. Cole, V.C. Yang, The artificial peroxidase activity of magnetic
805 iron oxide nanoparticles and its application to glucose detection, *Biomaterials* 30 (2009)
806 4716-4722.

807 [42] P.D. Liyanage, P. Weerathunge, M. Singh, V. Bansal, R. Ramanathan, L-Cysteine as an
808 Irreversible Inhibitor of the Peroxidase-Mimic Catalytic Activity of 2-Dimensional Ni-Based
809 Nanozymes, *Nanomaterials* 11 (2021) 1285-1298.

810 [43] F. Ma, H. Zhao, Optical, Magnetic, Ferroelectric Properties and Photocatalytic Activity
811 of $\text{Bi}_2\text{Fe}_4\text{O}_9$ Nanoparticles through a Hydrothermal Assisted Sol-Gel Method, *Russ. J. Phys.*
812 *Chem. A* 93 (2019) 2079-2086.

813 [44] J. Zhao, T. Liu, Y. Xu, Y. He, W. Chen, Synthesis and characterization of
814 $\text{Bi}_2\text{Fe}_4\text{O}_9$ powders, *Mater. Chem. Phys.* 128 (2011) 388-391.

815 [45] Z.-T. Hu, S.K. Lua, T.-T. Lim, Cuboid-like $\text{Bi}_2\text{Fe}_4\text{O}_9/\text{Ag}$ with graphene-wrapping tribrid
816 composite with superior capability for environmental decontamination: nanoscaled material
817 design and visible-light-driven multifunctional catalyst, *ACS Sustain. Chem. Eng.* 3 (2015)
818 2726-2736.

819 [46] Y. Wang, M. Daboczi, C.A. Mesa, S.R. Ratnasingham, J.-S. Kim, J.R. Durrant, S. Dunn,
820 H. Yan, J. Briscoe, $\text{Bi}_2\text{Fe}_4\text{O}_9$ thin films as novel visible-light-active photoanodes for solar
821 water splitting, *J. Mater. Chem. A* 7 (2019) 9537-9541.

822 [47] H. Yang, J. Dai, L. Wang, Y. Lin, F. Wang, P. Kang, A novel approach to prepare
823 $\text{Bi}_2\text{Fe}_4\text{O}_9$ flower-like spheres with enhanced photocatalytic performance, *Sci. Rep.* 7 (2017)
824 1-11.

825 [48] M.O. Amin, B. D’Cruz, M. Madkour, E. Al-Hetlani, Magnetic nanocomposite-based
826 SELDI probe for extraction and detection of drugs, amino acids and fatty acids, *Microchim.*
827 *Acta* 186 (2019) 1-10.

828 [49] L. Li, P. Ma, S. Hussain, L. Jia, D. Lin, X. Yin, Y. Lin, Z. Cheng, L. Wang, FeS_2 /carbon
829 hybrids on carbon cloth: a highly efficient and stable counter electrode for dye-sensitized
830 solar cells, *Sustain. Energy Fuels* 3 (2019) 1749-1756.

831 [50] B. Hu, J.-F. Wang, J. Zhang, Z.-B. Gu, S.-T. Zhang, Synthesis, structures and properties
832 of single phase BiFeO_3 and $\text{Bi}_2\text{Fe}_4\text{O}_9$ powders by hydrothermal method, *J. Mater. Sci.: Mater.*
833 *Electron.* 26 (2015) 6887-6891.

834 [51] Y. Du, Z. Cheng, S. Dou, X. Wang, Tunable morphology and magnetic properties of
835 $\text{Bi}_2\text{Fe}_4\text{O}_9$ nanocrystal synthesized by hydrothermal method, *J. Nanosci. Nanotechnol.* 11
836 (2011) 2691-2695.

837 [52] T.-J. Park, G.C. Papaefthymiou, A.R. Moodenbaugh, Y. Mao, S.S. Wong, Synthesis and
838 characterization of submicron single-crystalline $\text{Bi}_2\text{Fe}_4\text{O}_9$ cubes, *J. Mater. Chem.* 15 (2005)
839 2099-2105.

840 [53] X. Wang, M. Zhang, P. Tian, W. Chin, C. Zhang, A facile approach to pure-phase
841 $\text{Bi}_2\text{Fe}_4\text{O}_9$ nanoparticles sensitive to visible light, *Appl. Surf. Sci.* 321 (2014) 144-149.

842 [54] P. Salgado, V. Melin, D. Contreras, Y. Moreno, H.D. Mansilla, Fenton reaction driven
843 by iron ligands, *J. Chil. Chem. Soc.* 58 (2013) 2096-2101.

844 [55] C. Von Sonntag, Advanced oxidation processes: mechanistic aspects, *Water Sci.*
845 *Technol.* 58 (2008) 1015-1021.

846 [56] E.S. Henle, Y. Luo, S. Linn, Fe²⁺, Fe³⁺, and oxygen react with DNA-derived radicals
847 formed during iron-mediated Fenton reactions, *Biochemistry* 35 (1996) 12212-12219.

848 [57] M. Zhao, J. Huang, Y. Zhou, X. Pan, H. He, Z. Ye, X. Pan, Controlled synthesis of
849 spinel ZnFe₂O₄ decorated ZnO heterostructures as peroxidase mimetics for enhanced
850 colorimetric biosensing, *Chem. Commun.* 49 (2013) 7656-7658.

851 [58] M. Pooladi, I. Sharifi, M. Behzadipour, A review of the structure, magnetic and
852 electrical properties of bismuth ferrite (Bi₂Fe₄O₉), *Ceram. Int.* 46 (2020) 18453-18463.

853 [59] Y. Liu, C. Wang, N. Cai, S. Long, F. Yu, Negatively charged gold nanoparticles as an
854 intrinsic peroxidase mimic and their applications in the oxidation of dopamine, *J. Mater. Sci.*
855 49 (2014) 7143-7150.

856 [60] Y. Zhu, Z. Yang, M. Chi, M. Li, C. Wang, X. Lu, Synthesis of hierarchical Co₃O₄@
857 NiO core-shell nanotubes with a synergistic catalytic activity for peroxidase mimicking and
858 colorimetric detection of dopamine, *Talanta* 181 (2018) 431-439.

859 [61] J. Yin, H. Cao, Y. Lu, Self-assembly into magnetic Co₃O₄ complex nanostructures as
860 peroxidase, *J. Mater. Chem.* 22 (2012) 527-534.

861 [62] J. Lei, X. Lu, G. Nie, Z. Jiang, C. Wang, One-Pot Synthesis of Algae-Like MoS₂/PPy
862 Nanocomposite: A Synergistic Catalyst with Superior Peroxidase-Like Catalytic Activity for
863 H₂O₂ Detection, *Part. Part. Syst. Charact.* 32 (2015) 886-892.

864 [63] S. Dutta, C. Ray, S. Mallick, S. Sarkar, R. Sahoo, Y. Negishi, T. Pal, A gel-based
865 approach to design hierarchical CuS decorated reduced graphene oxide nanosheets for
866 enhanced peroxidase-like activity leading to colorimetric detection of dopamine, *J. Phys.*
867 *Chem. C* 119 (2015) 23790-23800.

868 [64] M.R.H. Nezhad, J. Tashkhourian, J. Khodaveisi, M.R. Khoshi, Simultaneous
869 colorimetric determination of dopamine and ascorbic acid based on the surface plasmon
870 resonance band of colloidal silver nanoparticles using artificial neural networks, *Anal.*
871 *Methods* 2 (2010) 1263-1269.

872 [65] J. Zhu, X. Peng, W. Nie, Y. Wang, J. Gao, W. Wen, J.N. Selvaraj, X. Zhang, S. Wang,
873 Hollow copper sulfide nanocubes as multifunctional nanozymes for colorimetric detection of
874 dopamine and electrochemical detection of glucose, *Biosens. Bioelectron.* 141 (2019)
875 111450-111466.

876 [66] H.W. Richter, W.H. Waddell, Mechanism of the oxidation of dopamine by the hydroxyl
877 radical in aqueous solution, *J. Am. Chem. Soc.* 105 (1983) 5434-5440.

878 [67] J.C. Barreto, G.S. Smith, N.H. Strobel, P.A. McQuillin, T.A. Miller, Terephthalic acid: a
879 dosimeter for the detection of hydroxyl radicals in vitro, *Lif Sci.* 56 (1994) PL89-PL96.

880 [68] Z. Xiang, Y. Wang, P. Ju, D. Zhang, Optical determination of hydrogen peroxide by
881 exploiting the peroxidase-like activity of AgVO₃ nanobelts, *Microchim. Acta* 183 (2016)
882 457-463.

883 [69] X. Lai, Y. Han, J. Zhang, J. Zhang, W. Lin, Z. Liu, L. Wang, Peroxidase-Like Platinum
884 Clusters Synthesized by Ganoderma lucidum Polysaccharide for Sensitively Colorimetric
885 Detection of Dopamine, *Molecules* 26 (2021) 2738-2751.

886 [70] M. Alam, B. Rao, E. Janata, OH reactions with aliphatic alcohols: evaluation of kinetics
887 by direct optical absorption measurement. A pulse radiolysis study, *Radiat. Phys. Chem.* 67
888 (2003) 723-728.

889